Draft version January 12, 2026
Typeset using LaTeX default style in AASTeX631

Simulating the formation of multiple populations in globular clusters: taking massive interacting binaries as the contaminants

Genghao Liu ,[1] Yunwei Deng,[2] Hui Li,[2] Baitian Tang,[3] Liubin Pan,[3] Long Wang,[3] Hongwei Ge,[4] and Alison Sills[5]

[1]School of Astronomy and Astrophysics, Sun Yat-sen University, Tangjiawan, Xiangzhou, Zhuhai, Guangdong, China
[2]TsingHua University, Haidian DS 100084, Beijing, China
[3]School of Astronomy & Astrophysics, Sun Yat-sen University, Tangjiawan, Xiangzhou, Zhuhai, Guangdong, China
[4]Yunnan Observatories, Chinese Academy of Sciences, Kunming 650216, People's Republic of China
[5]Department of Physics & Astronomy, McMaster University, 1280 Main Street West Hamilton, L8S 4M1, Canada

ABSTRACT

The ubiquitous presence of multiple stellar populations (MPs) in globular clusters implies strong and spatially inhomogeneous chemical self-enrichment, yet the physical mechanisms regulating its efficiency remain poorly quantified. We perform a suite of three-dimensional giant molecular cloud (GMC) simulations with the Arepo–RIGEL framework, incorporating chemically enriched yields from massive interacting binaries. Under typical conditions of isolated GMCs, even assuming maximized yields and the shortest enrichment timescales, the global mass fraction of second-population (2P) stars remains below $\sim 6\%$. Nevertheless, locally highly enriched stars can form, reaching [Na/Fe] values close to theoretical yield limits and producing nearly continuous abundance distributions consistent with observations.

We find that MP formation is governed by the interplay between stellar feedback, turbulent mixing, and pollutant transport. As a result, the 2P mass fraction exhibits a non-monotonic dependence on the initial GMC surface density, peaking near the Eddington surface density, and is anti-correlated with both the net heating timescale of cold dense gas and the transport timescale of enriched material into star-forming regions. Gravitational confinement enhances the conversion of feedback energy into turbulent motions, accelerating the turbulent cascade and shortening pollutant diffusion timescales. However, in excessively dense GMCs, efficient merging of feedback bubbles increases transport distances and suppresses 2P formation.

By modeling the time evolution of the pristine-abundance stellar fraction, we recover the same trend reversal and show that although higher surface densities shorten mixing timescales, the star formation duration decreases more rapidly. This competition limits the effective 2P formation window. Our results indicate that GMCs most favorable for MP formation are systematically denser than present-day Milky Way GMCs and are more consistent with high-redshift star-forming environments, providing physically motivated initial conditions for subsequent N-body studies of globular cluster evolution.

Keywords: methods: numerical – hydrodynamics - stars: formation – ISM: abundances – ISM: general – turbulence

1. INTRODUCTION

Globular clusters (GC), the oldest and most densely packed stellar systems in the universe, serve as unique windows into the star formation and chemical evolution of the early cosmos through their fossil stellar records(Raffaele G. Gratton et al. 2012; Gratton et al. 2004; Milone & Marino 2022; Renaud 2018; Gratton et al. 2019; Renzini et al. 2015). Since the first detection of CN-strong stars in M10 and M5 (Wayne Osborn 1971), a growing body of observations has confirmed the widespread presence of multiple stellar populations (MP) in globular clusters: these systems contain at least two distinct stellar subpopulations with different light-element abundances. The first population(1P) exhibits abundance patterns similar to coeval field stars, whereas the second population(2P) displays depletions in C, O, and Mg coupled with enhancements in N, Na, and Al, and typically exhibit higher helium abundances. Typically, the number ratio of 1P to 2P is about 1:1, these chemical anomalies are observed across various evolutionary stages, from the main sequence(MS) to red giants(RGB) and horizontal branch(HB) stars, indicating that they originate from pre-stellar enrichment of the interstellar medium rather than from internal stellar mixing. The ubiquity of MP and their complex correlations with cluster mass, metallicity, and dynamical environment make them a central, interdisciplinary challenge in contemporary studies of star formation, stellar evolution, and cluster dynamics.

Multiple generation scenarios is mainstream of the MP formation models. In this framework, the gas with 2P chemical pattern is produced through the H-burning within massive stars(able to activate CNO cycle, NeNa chain, MgAl chain, etc.), which evolve faster and would subsequently eject H-burning product into the interstellar medium. This enriched material mixes with pristine gas, eventually giving birth to 2P stars. However, this scenario has to face the traditional "mass budget" problems: how massive stars, the minority in stellar populations according to the initial mass function, could release sufficient enriched material to form about 1:1 1P/2P ratio? The discovery of "relative abundance" problem also require the polluters to be capable of flexibly adjusting the abundance ratios of alpha elements to helium to match the observational results of various globular clusters(Bastian et al. 2015).

Many polluter models have been proposed, such as asymptotic giant branch stars(AGB, Ventura & D'Antona 2009; D'Ercole et al. 2010; Doherty et al. 2014), fast rotating massive stars(FRMS, Bastian & Lardo 2018), very massive stars(VMS, Vink 2023), super massive stars(SMS, Denissenkov & Hartwick 2013; Gieles et al. 2018). Massive interacting binaries(MIB) stood out as one of the most promising candidates. This model posits that Roche-lobe overflow(RLOF) in Case-B mass transfer can significantly enhance the chemical yield. The maximum binary ejecta is more than the ejecta of AGB and FRMS combined(De Mink et al. 2009), and Michelle Nguyen & Sills (2024) found that MIB yields ~ 0.2 more than individual massive stars, averagely. Calculations from Binary_C(Robert G. Izzard & Tout 2003) proved that RLOF could significantly enhance wind mass loss by an order of magnitude after $\sim$ 6Myr(Yates et al. 2023).

How does MP form and evolve? Current numerical simulations have established a foundational paradigm: MP arise naturally through internal chemical self-enrichment during the formation of globular clusters. These simulations indicate that 2P stars form nearly concurrently with 1P stars(Howard et al. 2019; Lahén et al. 2023). To study long-term dynamical evolution and mass loss history of 1P and 2P populations, N-body simulations must assume their initial spatial distributions and number ratios(e.g. Vesperini et al. 2013; Lacchin et al. 2024). These assumptions constitute the decisive initial conditions that determine whether a globular cluster, having passed its long evolution history, can ultimately match the observed 2P fractions and specific spatial-kinematic differences(Aros et al. 2025; Livernois et al. 2024), but how to elegantly derive these initial conditions of infant globular clusters is still unclear. While current hydrodynamic simulations have made some progress, they remain insufficient to complete this relay. For instance, Lahén et al. (2023) quantified the relative contributions of stellar winds and supernovae to the enrichment of the interstellar medium, but the mass and size of the clusters simulated are significantly smaller than that of present-day GC. Howard et al. (2019) demonstrated through post-processing methods that injecting helium with a mass equivalent to a few percent of the cluster's total mass can reproduce the observed-level of MP, but the effect of turbulent mixing were not investigated in their models. A question that impedes the connection between the short-term formation and long-term evolution of GCs remains unresolved: given a GMC with specified mass, density, and metallicity, how many 2P stars can form under self-consistent star formation and intense feedback, and what are their initial spatial distributions?

On the other hand, the peculiar phenomena observed in high-Z star formation, such as strong nitrogen emission(e.g. Topping et al. 2024, 2025), UV excess(Jeong et al. 2024; Matzner 2024), Li et al. (2023) and the presence of massive stellar clumps(Claeyssens et al. 2023; Adamo et al. 2024), are drawing our attention to the significance of environmental conditions, because the MP are almost exclusively found in ancient GCs, but absent in young clusters. This preference strongly suggests that the MP formation is probably linked to the extreme physical conditions unique to the early universe.

Therefore, it is now more eager than ever to uncover the answer to that question. We aim to conduct the simulations that self-consistently couple the entire physical chain, investigating the formation of MP starting from the GMC with specified mass, density, and metallicity. Our paper is organized as follows. In Sec.2, we present the preview of the binary yield model. In Sec.3, we describe the setup of the simulations. In Sec.4, we present the basic information about star formation process of our simulations. We then present our analysis on how mixing and diffusion process affect MP formation in Sec.6 and provide the optimal GMC parameter space for MP formation. In Sec.7 we compare our results to previous works, discuss the implications of our results on the MP formation scenarios, limitations of our models and analysis.

2. METHODS

Simulations in this work are all performed on the framework of Arepo-RIGEL(Deng et al. 2024), Arepo is a moving-mesh, finite-volume quasi-Lagrangian hydrodynamic code, conserved variables in each Voronoi cell are evolved with a second-order, unsplit Godunov scheme, these cells can be refined and de-refined to meet resolution requirements, and the mesh-generating points (the seed that define the Voronoi tessellation) are free to follow the motion the fluid. AREPO therefore integrates the strengths of both grid-based and particle-based hydrodynamic methods and has already been applied to various astrophysical problems(Springel 2010; Vogelsberger et al. 2013; Weinberger et al. 2020; Torrey et al. 2012).

The RIGEL (Realistic ISM modeling in Galaxy Evolution and Lifecycles) model integrates individual massive-star feedback into AREPO-RT to model heating, cooling and chemical enrichment of the multiphase ISM. The radiation field is modeled in seven spectral bins ranging from IR to He II ionizing bands and used to evolve non-equilibrium chemistry of main ISM coolants (e.g., H, H2, C, O, CO) and compute, in real time, all coupled heating and cooling processes to produce a self-consistent per-cell net cooling rate. This enables RIGEL to capture the thermodynamics across all ISM phases, thereby simulating the entire process of star formation and feedback.

In the rest of this section, we demonstrate how we construct binary yield model base on Arepo-RIGEL.

2.1. *Binary Yield Model*

We sample binaries in Arepo-RIGEL using Primary-constrained pairing algorithm(Cournoyer-Cloutier et al. 2021): Once a star particle host a massive stars with mass $M = M_{fb}$, we draw a Uniform(0,1) random number and judge if it's smaller than a mass-dependant bianry fraction $F(M_{fb})$ to determine whether this massive star has an companion. If does, the period P and mass ratio q will be sampled sequentially. Therefore, the probability of a binary system in a stellar population having a specific primary mass $M_1 = M_{fb}$, period P and mass ratio $q = \frac{M_1}{M_2}$ is

$$F(M_1, P, q) = F(M_1)F(P|M_1)F(q|M_1P) \tag{1}$$

, where $F(M_1)$ is primary-mass-dependent binary fraction distribution, $F(P|M_1)$ is primary-mass-dependent period distribution, $F(q|M_1P)$ is primary-mass- and period-dependent mass ratio distribution. All these three distributions are based on the observational results from Moe & Di Stefano (2017), the detailed sampling procedure is shown in Appendix A. The parameter space of the binary population covers all the massive star mass sampled by RIGEL($M_1 \in [8M_\odot, 100M_\odot]$ is set in this work), period in log scale ranging 0.2-8, mass ratio ranging 0.1-1.

Mass transfer initiates when the primary star fills its Roche lobe (Chen et al. 2024). Chemically enriched gas is then transferred through the L1 Lagrangian point toward the secondary star, and ultimately expelled into the interstellar medium (ISM) due to the secondary's rapid rotation (De Mink et al. 2009). Approximately 80%-90% of the mass transfer is Case B mass transfer, i.e. the primary reaches the Roche limit before the onset of core helium burning(Van Den Heuvel 1969). We therefore define the onset of chemical enrichment as the time when the primary reaches the base of the giant branch (BGB), adopting the BGB timescale from Hurley et al. (2000):

$$t_{\rm BGB}(M, Z) = \frac{a_1 + a_2M^4 + a_3M^{5.5} + M^7}{a_4M^2 + a_5M^7}, \tag{2}$$

with coefficients a_i $(i = 1, 2, 3, 4, 5)$ provided in Appendix A (Table 2).

In RIGEL, massive stars are assumed to evolve instantaneously, with supernova ejecta released only at the end of their lifetimes (Vogelsberger et al. 2013; Deng et al. 2024). Accordingly, we adopt $t_{\rm BGB}$ as the RLOF yielding timescale. Once the age of a massive interacting binary reaches this timescale, it releases all its enriched ejecta into the ISM. The chemical yields are derived through interpolation from the binary yield tables presented by Michelle Nguyen & Sills (2024), which were computed using the MESA stellar evolution code (Paxton et al. 2019).

The interpolated ejected mass table of binaries in this work is shown in Figure 1. Note that the parameter space of the binary population we sampled extends beyond existing chemical yield tables (See Fig 2 and Fig 1). For binary systems outside the tabulated ranges, we avoid extrapolation and instead introduce a 'boost factor' parameter η to scale the ejecta mass. This addresses potential underestimation of binary enrichment due to incomplete parameter coverage or omitted physical processes like common envelope ejection. The interpolated binary systems account for

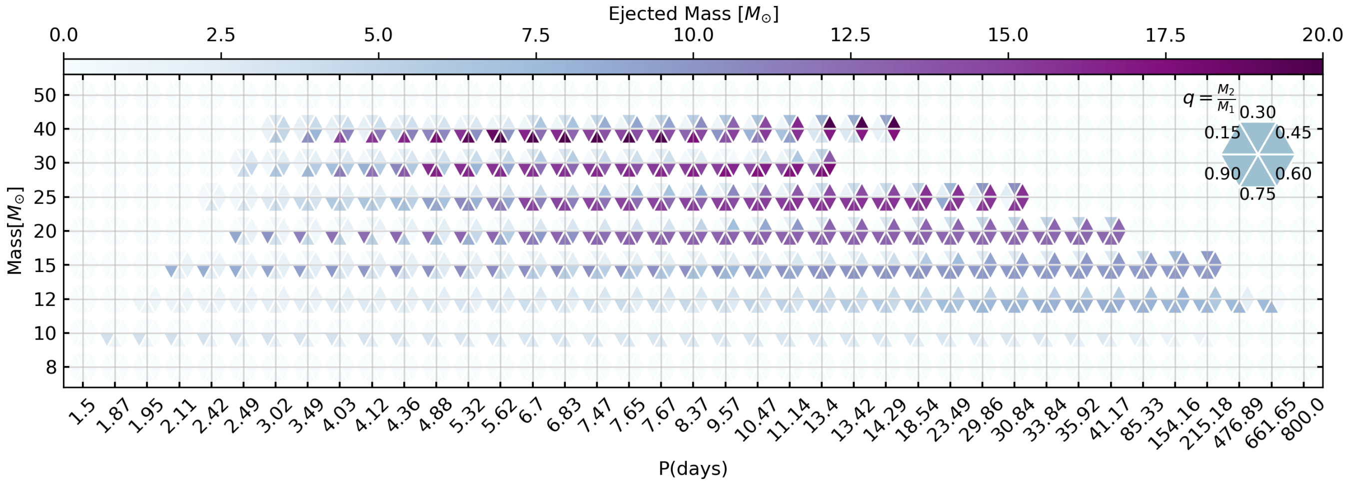

Figure 1. Interpolated ejected-mass table used in this work. Color scale shows the mass ejected by interacting binaries across the sampled parameter space. Horizontal axis: orbital period (log scale); vertical axis: primary mass. Each hexagon is subdivided into triangular wedges that encode different mass-ratio bins (legend at upper right). For example, the top-left triangular wedge denotes binaries with mass ratios in the range 0.15–0.30. The yields are interpolated from the MESA-based binary yield tables (see text); systems outside the tabulated ranges were treated using a boost factor to avoid extrapolation.

$\sim \frac{1}{3}$ of the total mass of all binaries whose periods <1500 days, and $\sim 14\%$ of the total sampled stellar mass(including single stars). These systems exhibit an average mass ejection fraction of $\sim 23\%$. Given that common envelope ejection typically releases $\sim 80\%$ of its total mass, assuming the entire stellar population could enrich material at this rate would yield an estimated boost factor of $\eta \sim 20$, which is expected to be the upper limit of the whole population's enrichment capacity.

2.2. *Post RLOF evolution*

After mass transfer through roche lobe overflow, binaries with different orbital parameter enter various evolutionary paths, and this post RLOF evolution could significantly affect the explodability and the intensity, timing and spatial distribution of stellar feedback and chemical enrichment(e.g. Laplace et al. 2021; Vartanyan et al. 2021; Wagg et al. 2025). In this work, we assume all binaries with current primary masses(i.e. primary after possible mass transfer) between 8 $M\odot$ and 40 $M\odot$ would explode and release ~ 1 Bethe (1 Bethe$\equiv 10^{51}$erg) thermal energy(See Deng et al. 2024), and before which, we utilize 4 mass transfer criteria to evaluate the change made by binary interaction to the orbit parameters, shown in the following subsection.

2.2.1. *Mass transfer criteria*

Mass transfer and its stability determine the fates of the binary(Chen et al. 2024; Soberman & Phinney ????; Temmink et al. 2023), and the stability of the mass transfer are determined by the response of the primary radius under certain conditions to mass transfer versus the response of the roche lobe radius, which are

$$\zeta_{\rm ad} = \left(\frac{d\ \ln{\rm R}}{d\ \ln{\rm M}}\right)_{\rm ad}, \zeta_{\rm th} = \left(\frac{d\ \ln{\rm R}}{d\ \ln{\rm M}}\right)_{\rm th}, \zeta_{\rm L} = \frac{d\ \ln{\rm R_L}}{d\ \ln{\rm M}}, \zeta_{\rm L2} = \frac{d\ \ln{\rm R_{L2}}}{d\ \ln{\rm M}} \tag{3}$$

where R,$\rm R_L$,$\rm R_{L2}$ denote radius of the donor(primary stars in this work), L1 point radius, L2 point radius, respectively, subscripts 'ad' and 'th' denote adiabatic and thermal equilibrium condition, respectively. Only when the radius of the primary contract more slowly or expand more rapidly than roche lobe radius, i.e. $\zeta_x(q) > \zeta_{\rm L}(q)(x = {\rm ad}, {\rm th})$[1], could mass transfer be sustainable. In our model, we employs three critical mass ratios q_{ad}, q_{th}, q_{L2}, which serve as the thresholds for triggering dynamical-timescale mass transfer, thermal-timescale mass transfer, and the overfilling of the outer Lagrangian surface(See Ge et al. 2010, 2020a, and the reference therein), to categorize the entire binary

[1] Given conservative or constant fractional non-conservative mass transfer, mass–radius relations can be written only by the initial mass ratio q.

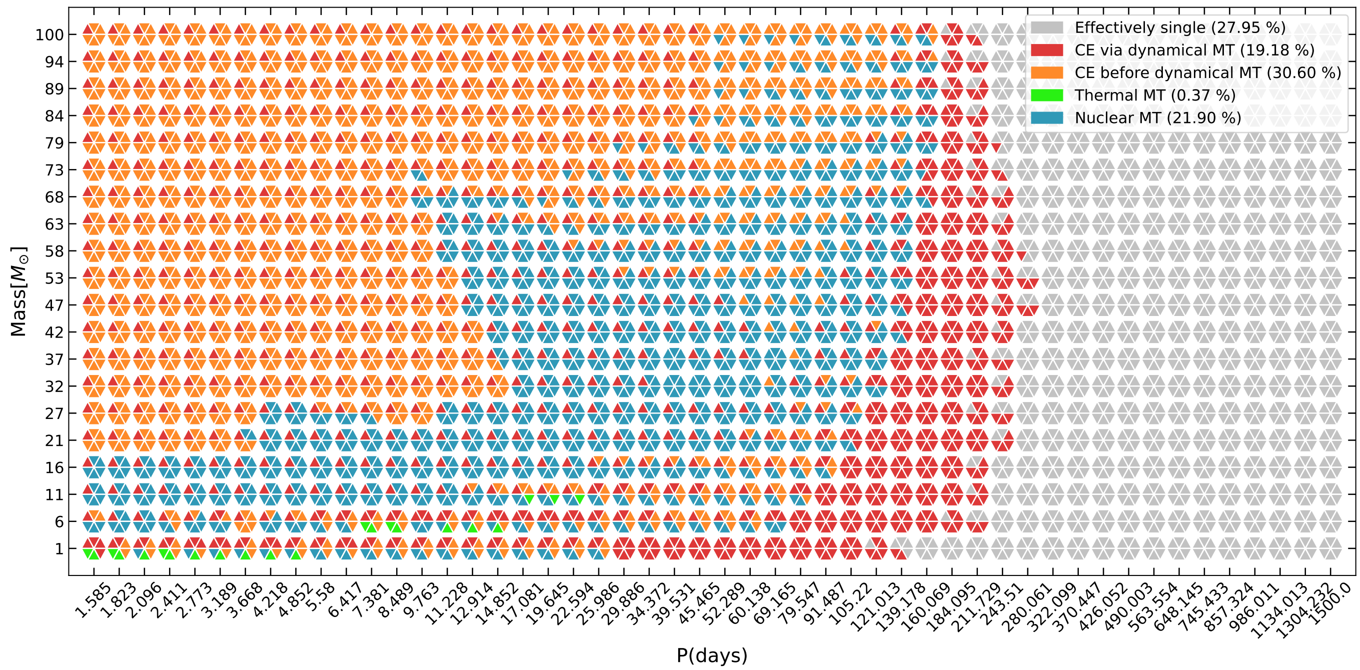

Figure 2. Map of mass-transfer timescales (dominant evolutionary channel) for binaries with orbital period P < 1500 days. Regions are color-coded by the predicted timescale/channels determined by the critical mass ratios q_{ad},q_{th} and q_{L2} adopted in this work(see Section 2.2.1 for detail).

population into four distinct evolutionary channels. To distinguish between the conventional definition of mass ratio used in mass transfer studies and that employed in this work, we define the mass ratio in terms of the donor to accretor mass as $\tilde{q} = \frac{M_{donor}}{M_{acc}} = \frac{1}{q}$, then the four evolutionary pathways are classified as follow:

- if $\tilde{q} > q_{\rm ad}$, mass transfer will proceeds on a dynamical timescale, and form a common envelope(CE) during mass transfer.

- if $q_{\rm L2} < \tilde{q} < q_{\rm ad}$, the mass transfer will be stable and proceeds on a thermal timescale with a common envelope formed by L2-overflow. This process will also form a CE.

- if $q_{\rm th} < \tilde{q} < \min(q_{\rm L2}, q_{\rm ad})$, the mass transfer will be stable and proceeds on a thermal timescale. We assume this channel could form a binary-stripped star(He star) plus a accreted MS system.

- if $\tilde{q} < q_{\rm th}$, the mass transfer will be stable and proceeds on a nuclear timescale. We assume this channel could also form a He+MS system.

- For those binary which will not interact before SNe, we expect that they do not have any differences with single stars, so our model treat them as single stars.

Critical mass ratio tables are adopted from Ge et al. (2020b, 2024), including thermal-timescale mass transfer and unstable mass transfer overfilling outer Lagrangian point, dynamical-timescale mass transfer in fully conservative, semi-conservative, and fully non-conservative cases. We interpolate these critical mass ratio tables and build the corresponding evolution channels of binary population based on them(See Figure 2 for a review).

Consequently, mass transfer yields remanent objects like binary-stripped stars, accreted MS companions, and CE systems including those undergoing subsequent CE ejection or coalescence, all of whose evolution deviate significantly from that of their primordial single-star. However, a comprehensive, population-wide model that tracks their later evolution and quantifies their cumulative impact on stellar feedback and chemical enrichment is still lacking. Note that in this work we focus only on the pre-supernova chemical yields of massive interacting binaries, rather than the detailed fate of their remnants, so we no longer distinguish the individual binaries after their explosion. In addition, the assumption that all primaries with masses between $8M_{\odot}$ and $40M_{\odot}$ will eventually undergo core-collapse supernovae is basically justified because stars in this range generally form massive enough helium or carbon–oxygen cores to trigger either Type II or stripped-envelope (Ib/Ic) explosions, releasing comparable explosion energies(See Sec7.2.1 for more discussion). The key role of binary evolution in our context is therefore not whether, but when a supernova occurs. Binary interactions through accretion, rejuvenation, or envelope stripping can substantially modify stellar lifetimes and the onset of supernova feedback. Rejuvenation replenishes nuclear fuel in the core via rotational or mixing processes, extending the lifetime of the primary (e.g., Wagg et al. 2025; Lynnette M. Dray & Christopher A. Tout 2007; Schneider et al. 2016). In the following subsection, we show how we estimate the expected supernova timescales for the different evolutionary channels considered in our model.

2.2.2. *SNe timescale determination*

Binary interactions such as rejuvenation and envelope stripping can delay SN feedback in massive stars. The former achieves this by replenishing the fuel supply of nuclear reaction in the cores through internal chemical mixing, which in turn extends the stellar lifetime (e.g., Wagg et al. 2025; Lynnette M. Dray & Christopher A. Tout 2007; Schneider et al. 2016). The latter achieves this by producing a remnant envelope-stripped helium core with lower compactness and a steeper density profile, which will also alter their explodablity and SN energy(Laplace et al. 2021; Vartanyan et al. 2021; Gutcke et al. 2021; Steinwandel & Goldberg 2025). Mergers-, accretion-, and rotation-induced chemical mixing can cause stellar rejuvenation, to varying extents. For the merger in our model, we adopt the scheme of Glebbeek et al. (2013), which is

$$\phi = C\frac{q}{(1+q)^2}\frac{R_{1,0.86}+R_{2,0.86}}{R_{1,0.5}+R_{2,0.5}} \tag{4}$$

$$f_{app} = \frac{1}{Q_c(M)}\frac{1}{1-\phi}\frac{Q_{c,1}f_1+Q_{c,2}f_2 q}{1+q} \tag{5}$$

$$t_{MS} = \tau_{MS}(1-\frac{f_{app}}{\alpha}) \tag{6}$$

where $R_{n,0.86}$ and $R_{n,0.5}$ are the radii containing 86 and 50 percent of the mass of parent star n (1 for the primary and 2 for the secondary). Here we assume $\frac{R_{1,0.86}+R_{2,0.86}}{R_{1,0.5}+R_{2,0.5}} = 1$ and $C = 0.3, \alpha = 1.67$ for $M < 2.4M_\odot$; $C = 0.35, \alpha = 1.14$ for $M >= 2.4M_\odot$ according to the simulations from Glebbeek et al. (2008); Schneider et al. (2016); Glebbeek et al. (2013). We assume a fully mixed of the new stars and hence we can derive a new metallicity by

$$Z_{\rm new} = \frac{Z_{\rm old}{\rm M}_2 + {\rm M}_{\rm He,acc}}{{\rm M}_2} \tag{7}$$

, where $Z_{\rm old}$ is the metallicity before mass transfer, $\rm M_{He,acc}$ is the He mass of accreted mass.

For accretion cases, the secondary will become primary in the new binary system if its mass exceed the previous primary, and the new binary particle will inherit the age of its progenitor and rejuvenated following the scheme adopted from Lynnette M. Dray & Christopher A. Tout (2007):

$$t' = \frac{M}{M'}\frac{\tau'_{MS}}{\tau_{MS}}t \tag{8}$$

and the new metallicity will be estimated by

$$Z_{\rm new} = \frac{{\rm Y} + {\rm M}_{\rm He,acc}/{\rm M}_2}{2 + 2{\rm M}_{\rm acc}/{\rm M}_2} - 0.12 \tag{9}$$

,where Y is the initial Helium abundance of the secondary.

Thus, primary masses, periods, mass ratios, metallicities and ages of all massive binary stars will be updated after BGB time(Eq.2) according to their own binary evolution channels, and proceed their subsequent evolution until CCSNe.

3. INITIAL CONDITIONS

We use MakeCloud(Grudić & Guszejnov 2021) to generate a series of uniform density distributed giant molecular clouds(GMC) as the progenitor of globular clusters. The GMCs are initialized in a sub-virial state characterized by virial parameters $\alpha_0 \sim 0.8$, supported by turbulent velocity instead of initial rotation. These GMCs are expected to

Table 1. Initial conditions of GMCs.

Name	M	R	$t_{\rm ff}$	ρ_0	Σ_0	α_0	L	η	$\Delta m_{\rm gas}$	$f_{\rm 2P}$
Units	$M_\odot$	pc	Myr	$M_\odot/pc^3$	$M_\odot/pc^2$				$M_\odot$	%
M1e7R15L0E1	1e7	15	0.29	707.36	14147.11	0.79	0	1	1.0	0.147
M1e7R30L0E1	1e7	30	0.83	88.42	3536.78	0.79	0	1	0.5	0.559
M1e7R30L0E20	1e7	30	0.83	88.42	3536.78	0.78	0	20	2.0	2.270
M1e7R47L0E1	1e7	47	1.63	22.99	1440.97	0.79	0	1	1.0	0.160
M1e6R15L0E1	1e6	15	0.93	70.74	1414.71	0.77	0	1	0.5	0.575
M1e6R20L0E1	1e6	20	1.43	29.84	795.77	0.77	0	1	1.0	0.135
M1e6R30L0E1	1e6	30	2.63	8.84	353.68	0.79	0	1	1.0	0.130
M1e5R15L0E20	1e5	15	2.94	7.07	141.47	0.79	0	20	1.0	3.624
M1e5R15LNE20	1e5	15	2.94	7.07	141.47	0.79	N	20	1.0	0.000
M1e6R50L0E1	1e6	50	5.66	1.91	127.32	0.79	0	1	1.0	0.143
M1e6R50L0E20	1e6	50	5.66	1.91	127.32	0.79	0	20	1.0	3.803
M1e7R200L0E1	1e7	200	14.31	0.30	79.58	0.78	0	1	1.0	0.091
M1e7R200L0E20	1e7	200	14.31	0.30	79.58	0.78	0	20	1.0	5.790
M1e6R100L0E1	1e6	100	16.00	0.24	31.83	0.79	0	1	1.0	0.011
M1e6R100L0E20	1e6	100	16.00	0.24	31.83	0.79	0	20	1.0	5.512

NOTE—Column information from left to right: model name, initial GMC mass M, initial GMC radius R, initial free-fall time $t_{\rm ff}$, initial density ρ_0, initial surface density Σ_0, initial virial parameter for the rotational components α_0, yield lag L, Enrichment boost factor η, target mass for gas cells Δm_{gas}, 2P mass fraction $f_{\rm 2P}$(Eq.12).

trigger internal mass redistribution from uniform to centralized distributions without large scale contraction, ultimately leading to stellar formation through turbulent fragmentation(e.g. Xu & Lazarian 2020; Murray et al. 2017; Murray & Chang 2015). The turbulent spectrum follows a Kolmogorov-type scaling with spectral index 2.0, implemented through balanced solenoidal and compressive modes to replicate observed inertial-range turbulence. The gas temperature is initialized to 10 K, which is commonly used for GMC simulations(Li et al. 2019; McKee & Ostriker 2007; Julia Roman-Duval et al. 2010). For the initial chemical composition we adopt an alpha-enhanced abundance pattern following Michelle Nguyen & Sills (2024), characterized by metallicity [Fe/H] $= -1.44$, [O/Fe] $= 0.44$, $Z = 1.2 \times 10^{-3}$ and $Y = 0.25$.

We employ a RSLA(Reduced Speed of Light Approximation, see Gnedin & Abel 2001, for review) factor of 0.001, i.e. $\tilde{c} = 0.001c$, to increase the efficiency without introducing significant numerical errors(Rosdahl et al. 2013). We also employ the spatial resolution correction methods outlined by Deng et al. (2023) to ensure the feedback effects converge correctly across different simulation resolutions.

All relevant physical parameters characterizing these initial conditions are tabulated in Table 1. We varied the masses and radii of the GMCs to explore the their relations to multiple stellar populations. Deng et al. (2024) enforced an instantaneous star formation when the length of the gas cell is larger than half of its local jeans length, i.e. $m_{gas} > f_{j,s}^3 M_J$, where $f_{j,s} = 0.5$, violation to which would cause the artificial fragmentation. Here we follow their settings and chose mass resolutions to ensuring all the gas cells would not violate that sufficient condition at the very beginning of the simulation. We mammally revise the yielding timescale with a yield lag "L", which denotes the time of yielding after their birth, and the enrichment from individual binary systems allows for amplification by a boost factor η(See 5 for details).

4. STAR FORMATION

We simulated the star formation of 14 GMC varying masses, radii, chemical yield boosting factors, until they quench, typically at least twice of free fall times, $\sim 2t_{\rm ff}$(See Li et al. 2019; Ni et al. 2025, and Fig. 4).

A visualization of star cluster formation is shown in Figure 3. No global contraction is observed in this GMC during the whole star formation process, stars form in the dense filaments and fragments instead of center dense clumps, this behavior is normal in uniform initial density profile, and is consistent with many simulations(e.g. Li et al. 2019; Shi et al. 2025; Birka Zimmermann et al. 2025). At ~ 1.37 Myr, turbulent velocity field dominates the formation of complex filamentary structures, causing early star formation (white dots) along the filaments and within

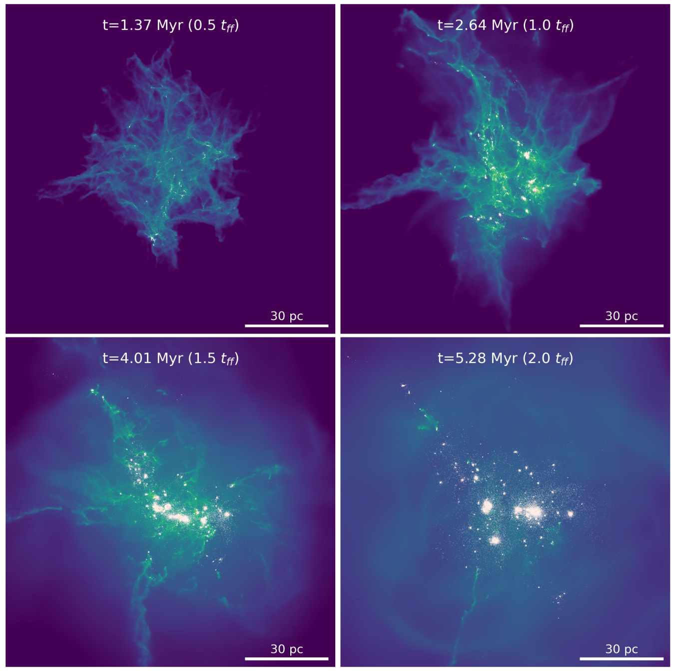

Figure 3. Four-panel visualization of star cluster formation in a representative GMC at successive times (upper-left to lower-right): 1.37 Myr, 2.64 Myr, 4.01 Myr, and 5.28 Myr. Panels show the gas/projected structure and star-particle locations; early star formation appears along filaments and in off-center dense clumps, sub-clusters form and hierarchically merge, and by the final time most gas has been expelled by feedback (bubbles visible). Star particles are color-coded by [Na/Fe]; 2P stars ([Na/Fe] > 0.3) would be pure red but are too rare ($\sim 1\%$) to be prominent in this visualization.

dense clumps at off-center locations(Upper left). At ~ 2.64 Myr, the high-density regions are compressed further, and several stellar sub-clusters hierarchically form and merge, the star formation comes to its peak. At ~ 4.01 Myr, more sub-clusters form and merge at the center of the star-cloud complex, while stellar feedback start to destroy the filamentary structures. At ~ 5.28 Myr, almost all the gas is expelled by the stellar feedback at this stage, filamentary structures are all destroyed, some bubbles are shown in lower right panel. The stars are color-coded by their [Na/Fe], 2P stars([Na/Fe]>0.3) will be marked as pure red, however they are too few($\sim 1\%$) to seen in this figure.

Figure 4 shows the star formation histories of the GMCs. Star formation histories for most of the GMCs are similar to Li et al. (2019). All GMCs in this study exhibit star formation histories following a triangle-shape, This manifests as a linear proportionality between early star formation rate and time, aligning with the theoretical predictions by Murray & Chang (2015) regarding star formation evolution under self-gravity. Star formation duration $\tau_{\rm dur} \sim 2t_{\rm ff}$, and integrated star formation efficiency $\epsilon_{\rm int}$ of all GMCs are similar to what Li et al. (2019) predicted. The time when SFR start and their peaks might be sensitive to the initial surface densities. Integrated $\epsilon_{\rm int}$ versus initial surface density is shown in Fig 5, red solid line with 68% confident range(shown in orange translucent band) is fitted using the formula in Li et al. (2019) and obtain the parameter $f_{\rm boost} = 5.326^{+0.979}_{-0.819}$.

$$\epsilon_{\rm int} = \frac{\sqrt{\Gamma^2 + (4\beta - 2)\Gamma + 1} - (2\beta - 1)\Gamma - 1}{2(1-\beta)\Gamma}. \tag{10}$$

where $\Gamma \equiv \Sigma_{\rm sh}/\Sigma_{\rm crit} = \pi G \Sigma_0 / 4 f_{\rm boost} \hat{p_w}$, $\beta = 1.83 \pm 0.89$, and the critical surface density defined by

$$\Sigma_{\rm crit} = \frac{\dot{p}}{\pi G} = \frac{\dot{p_w} f_{\rm boost}}{\pi G} \tag{11}$$

where $\dot{p_w} = 3.32 \times 10^9 {\rm cm/s^2}$ is the IMF- and time-averaged momentum deposition rate per unit mass, adopted from Li et al. (2019) fitted results; f_{boost} is a boosting factor of feedback. Note that in the language of Lancaster et al. (2021a,b); Thompson & Krumholz (2016); Raskutti et al. (2016); Fall et al. (2010), their critical surface density(or Eddington surface density $\Sigma_{\rm Edd}$ in their works) shares the same physical meaning as the one defined in this study, yet exhibits a subtle mathematical distinction, namely $\Sigma_{\rm crit} = 4\Sigma_{\rm Edd}$.

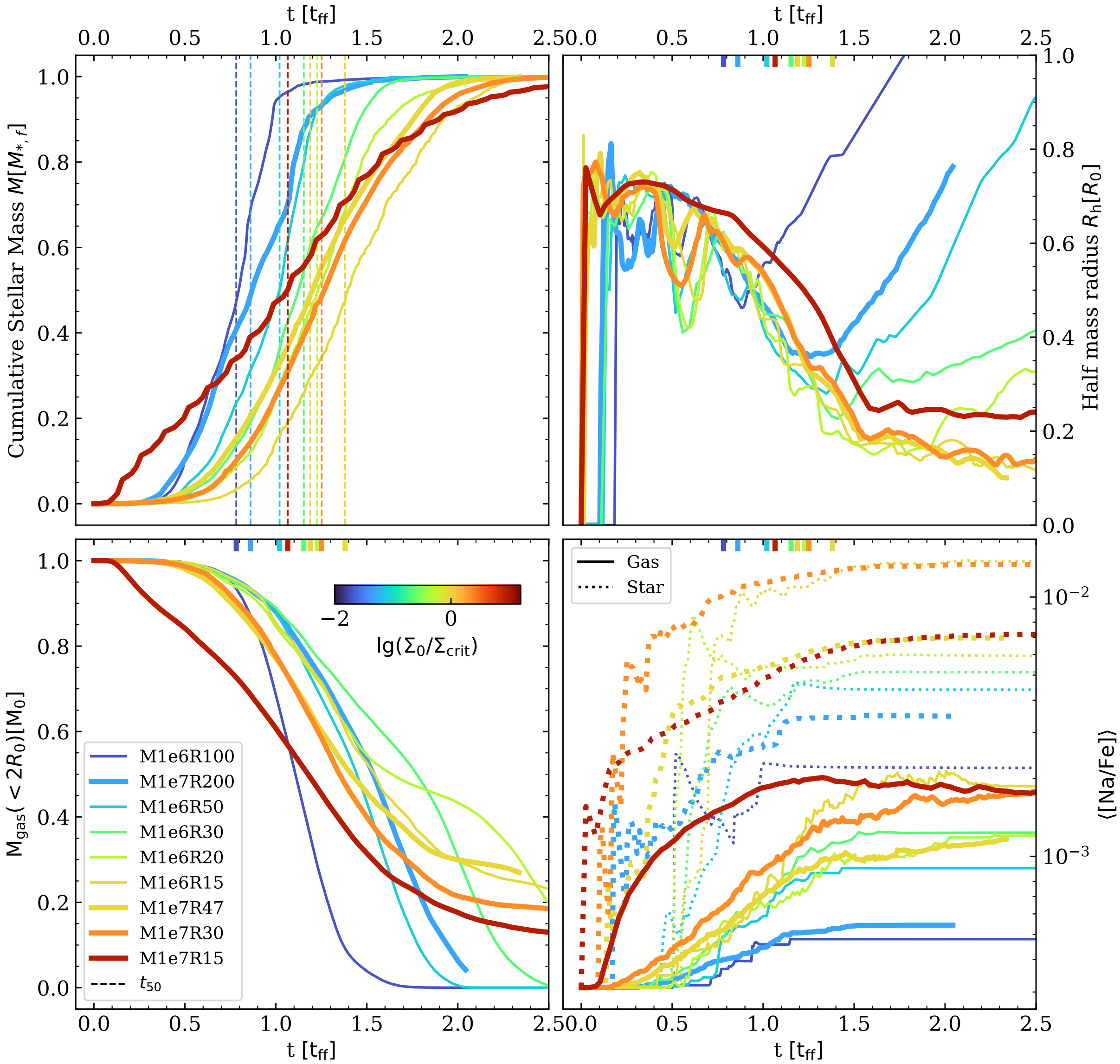

Figure 4. Star formation histories for the suite of GMC simulations. Most runs show a 'triangle' pattern (linear rise to a peak near $\approx t_{\rm ff}$ followed by a decline), with typical star-formation durations $\tau_{\rm dur} \sim 2t_{\rm ff}$. Differences in onset time and peak are driven by initial surface density and other initial conditions (see text).

5. THE FORMATION OF SECOND POPULATION

5.1. *Time Budget*

Following the convention of previous observational and numerical studies (e.g., Carretta et al. 2009; Lahén et al. 2024), we define 2P stars as those whose [Na/Fe] > 0.3 dex. In our fiducial star formation simulations, we observe a complete absence of 2P stars formed. This null result is physically consistent with the anti-correlation between star formation duration (SFD) and star formation efficiency(SFE), a relationship well-documented in the literature(Grudić et al. 2018; Li et al. 2019; Ostriker & Kim 2022), etc. As is mentioned above, the average yielding timescale of the yield table is ~ 12 Myr, with the earliest yielding timescale of ~ 6 Myr. For the GMCs whose star formation duration is shorter than the minimum binary yielding timescale, The time it takes for a GMC to reach the peak of its star formation activity is approximately one free-fall time, and the star formation duration is about twice the free-fall time(Ni et al. 2025). So we see at 3.2 Myr, the gas in GMC was expelled and star formation stop, but there's no 2P

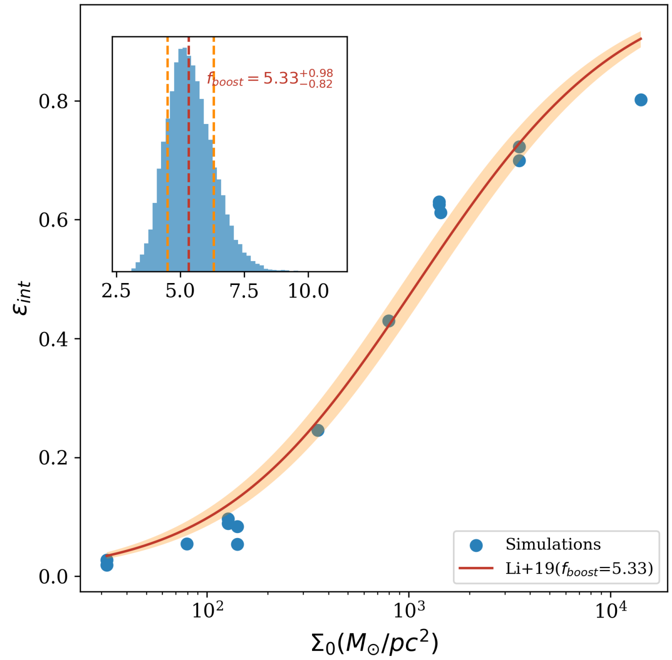

Figure 5. Integrated star-formation efficiency ϵ_{int} for all runs as a function of initial gas surface density Σ_0. The red solid line is the fitted relation following Li et al. (2019) and the orange band shows the 68% confidence interval from the MCMC fit; the fitted boost parameter is $f_{\rm boost} = 5.326^{+0.979}_{-0.819}$.

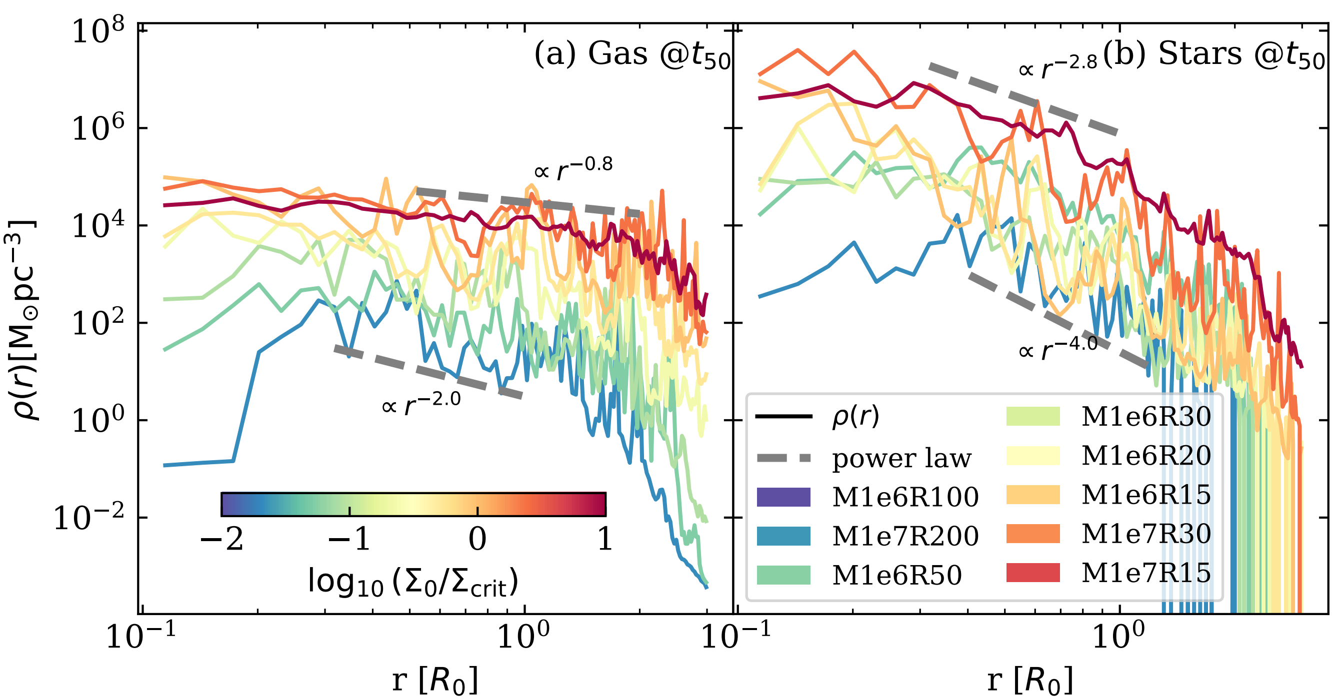

Figure 6. Radial density profile of gas(left) and stars(right) at the time when 50% stellar mass assembly, color-coded by initial surface densities of each simulations. gray thick dash lines show the power law scaling.

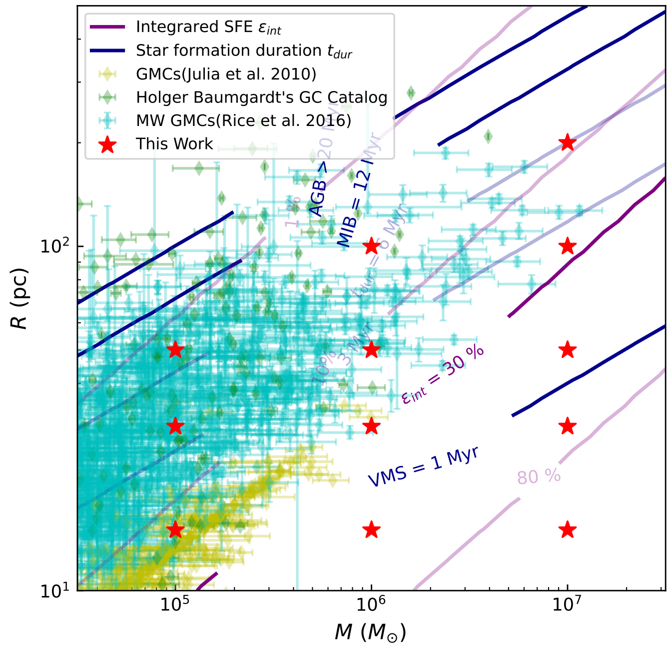

Figure 7. Initial parameter space for GMCs. Red contours: Integrated star formation efficiency ϵint. Blue contour: Star formation duration $\tau_{\rm dur}$ and the corresponding yielding timescale of different scenarios(AGB,VMS,MIB).Yellow dots denote the MW GMCs located within sun circle, provided by Julia Roman-Duval et al. (2010), cyan dots denote the MW GMCs in all locations, provided by Rice et al. (2016).

material released until about 6 Myr. And if the free fall time is larger than yielding time. here's an example, too few star formed in 6 Myr, so the enrichment in gas is not significant until 20 Myr.

Figure 7 demonstrates a so-called "Time Budget" dilemma: the mismatch between the star formation duration, star formation efficiency and the yielding timescale. Producing substantial 2P material demands higher SFE, but for isolated GMC, Denser clouds have higher SFE, it also lead to a shorter free fall time the stronger stellar feedback disrupts the cloud more rapidly, inevitably shortening the SFD. This shortened timescale leaves insufficient time window for the release and mixing of enriched ejecta with pristine gas, and its subsequent settling into new stars. The GMCs that can simultaneously satisfy high SFE(typically $\varepsilon \gtrsim 0.33$ for the survival of infant GC, see Baumgardt & Kroupa 2007) and the SFD long enough for MIB yielding timescale, this GMC must be extremely massive and large(See Figure 7).

In our study, we employ massive interacting binaries (MIB) as the primary enrichment source, which can inherently shorten the enrichment timescale through efficient mass transfer and binary interactions that accelerate ejecta release. The emergence of zero 2P stars in this work is not due to limitations of the MIB scenario itself, but rather arises from incomplete stellar evolution tables, insufficient coverage of mass ranges in the models, and constraints in computational resources. These factors reflect broader limitations in binary evolution theory and enrichment modeling. As mentioned in Section 3, we introduce a 'yield lag' parameter to explicitly control the enrichment timescale, enabling more flexible adjustment of the timing of ejecta incorporation. This approach sets the stage for the next section, where we detail the implementation of the yield lag parameter and its impact on simulation outcomes.

To maximize the enrichment time window, in some simulations, we artificially forced stars to release pollutants immediately upon their birth (marked as "L0") and boosted the yield mass by a factor of twenty (marked as "E20"; see Table 1 for details). The L0 setting aims to extend the time available for enrichment by eliminating delays, while E20 elevates the enrichment mass to the upper limit of the mass range, ensuring maximum material for 2P formation. These adjustments allow us to investigate the conditions that favor the incorporation of 2P gas into stars, which will be explored in the next chapter on mass budget, focusing on how specific parameters influence 2P enrichment efficiency.

5.2. *Mass Budget*

Figure 8 shows some basic properties of multiple populations in the newly formed star clusters. We expect that giant

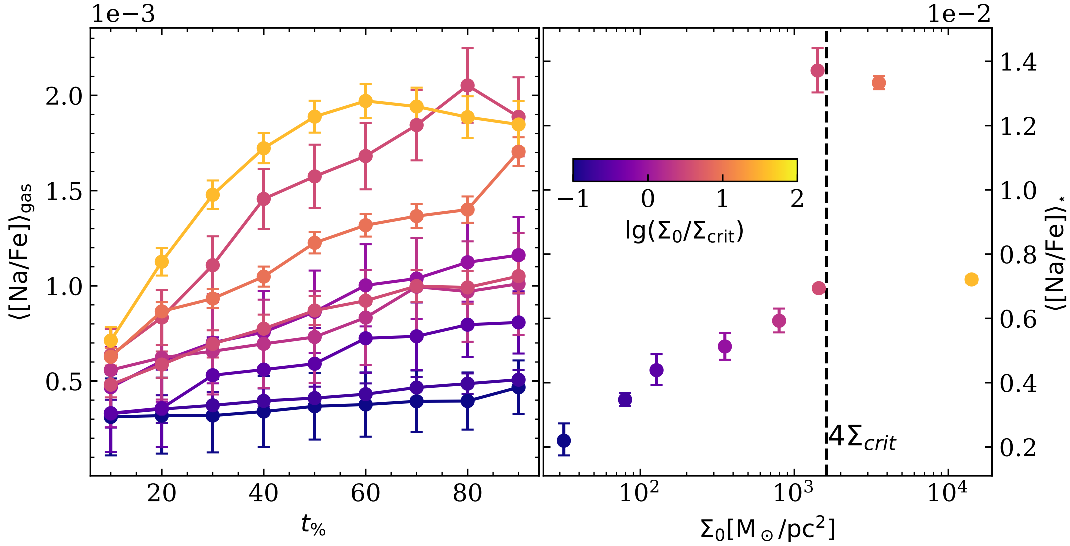

Figure 8. Summary of multiple-population metrics across the simulation suite. Plotted quantities include the 2P mass fraction (defined as mass fraction of star particles with [Na/Fe] > 0.3) and the mean stellar [Na/Fe] as a function of initial surface density; runs with immediate yielding (L0) and boosted yields (E20) are highlighted. Error bars (where shown) are estimated via bootstrap. The figure demonstrates a peak in mean [Na/Fe] near 4 times critical surface density $4\Sigma_{\rm crit}$ (see the text).

molecular clouds with tag "L0E20" and highest surface density will represents the upper limit of the number ratio of second-population (2P) stars. Note that star particles in RIGEL do not represent individual stars but rather subsets of the overall stellar population, the term "number of star particles" may be conceptually misleading. Therefore, we define the 2P ratio as the mass fraction of star particles with [Na/Fe] > 0.3 relative to the total stellar mass, i.e.,

$$f_{\rm 2P} = \frac{M_\star([{\rm Na/Fe}]_i > 0.3)}{M_\star} \tag{12}$$

, if we assume 1P and 2P stars share the same mass function, this mass-based ratio is equivalent to the number ratio of 2P to total stars. Additionally, we introduce the mean stellar Na abundance as a continuous metric to quantify the amount of enriched gas that goes into stars, defined as

$$\langle[{\rm Na/Fe}]\rangle_\star = \lg\left(\frac{\sum_i {\rm N_{Na,i}}}{\sum_i {\rm N_{Fe,i}}}\right) - [{\rm Na/Fe}]_\odot \tag{13}$$

, where $\rm N_{Na,i}$ and $\rm N_{Fe,i}$ are the total number of Na and Fe in i-th star particle, respectively. the 2P ratios still rarely exceeded $\sim 6\%$ in isolated GMCs (See Table. 1). If considered a typical star loss fraction of two-thirds(Baumgardt & Hilker 2018), 2P ratio is still much lower than the order of observations. The mean [Na/Fe] of the whole simulation suits ranging from $0.002 - 0.1$ dex.

Figure 8 demonstrates the relation between the initial surface density and the mean stellar Na abundance. For those GMCs with surface density below the marked $\Sigma_{\rm crit}$ (dashed line), the rise in $\langle$[Na/Fe]$\rangle$ is monotonic and gradually (from ~ 0.2 at $\Sigma_0 \sim 10$ M$_\odot$pc^{-2} to $\sim 0.5 - 0.6$ at $\Sigma_0 \sim 10^2$M$_\odot$pc^{-2}. A sharp leap of the trend and the maximum mean stellar Na abundance of this series of simulations appear at $\sim \Sigma_{\rm crit}$. Note that this abundance leap is not coupled with surface density merely, because there is another GMC M1e7R47L0E1 which share the same Σ_0 with the peak simulation M1e6R15L0E1 but remains slight increase compare to the lower Σ_0 GMC. Error bars estimated by bootstrapping confirm the truly existence of this abundance peak. Deep connection linking the global IC of GMCs to the mean stellar Na abundance will be discussed in Section 6.

Figure 6 (a) and (b) shows the radial density profile at t_{50} of gas and stars, respectively. The profile are centered at the mass center of the star-gas complex, both the gas and stellar profiles are normalized to the central stellar density of the corresponding run. We find that, denser GMCs seems have more flatten gas and stellar density profile when the same star-formation process has reached. The slope of gas profile ranging from -2 at diffuse end($\Sigma_0 \sim 10$ M$_\odot$/pc^2) to -0.8 at dense end($\Sigma_0 \sim 700$ M$_\odot$/pc^2), this trend is consistent with the observed radial profiles of star-forming molecular clumps(Csengeri et al. 2017). The slope of stellar density profile range from -4 to -2.8. Note that we did not find significant non-uniform radial distribution of f_{2P}, nor the discrepancy of velocity distribution between 1P and 2P stars, which imply that the two populations could not form with distinct dynamical features in isolated GMCs during a single star formation event(See Sec.7).

The stellar [Na/Fe]–[O/Fe] distribution is characterized by a dominant 1P base at O enriched and Na depleted zone plus a extended enriched 2P tail; As is shown in Fig.9 and Fig.10, blue symbols denote the original enrichment scenario while red ones indicate the enrichment boosted by a factor of 20, and the red stars show the maximum, mean and minimum yielded [Na/Fe] ; the colored error bars and dash lines in the right histogram are the [Na/Fe] range predicted by instantaneous dilution model (see Section 6.1); Only M1e5R15L0E20(Not shown here) and M1e6R100L0E20(Fig.9) display a bimodal distribution in [Na/Fe], and isolated clumps at the high-Na end, and these discontinuities in abundance distribution would naturally arise when star form in inhomogeneously mixed star-forming clumps. Stellar clusters form from low-Σ_0 GMCs tend to exhibit a relatively flat 2P tail in Na-O plane; in such clusters inefficient mixing produces discrete 2P subpopulations, in agreement with the observations. By contrast, higher-surface-density GMCs display a high-[Na/Fe] tail whose frequency falls off rapidly toward higher enrichment, indicative of more thorough mixing. The abundance extrema(maximum-minimum) ranging from 0.7-1.1 dex, with an outlier of M1e6R100E1($\sim$ 0.3 dex), whose Σ_0 is too low to create pollutants that yields high [Na/Fe] gas, this result imply that an absolute abundance ceiling does not by itself rule out MP formation models; the remaining challenge is primarily the 1P/2P number ratio. Under the most favorable timing for enrichment (i.e., enrichment occurring immediately after star formation), stellar [Na/Fe] can reach 4–7 times the gas-phase value; if the mass of enriched material is increased while the polluter spatial distribution is held fixed, this amplification can reach factors of tens. Denser GMCs show higher utilization efficiencies of enriched material: GMCs at or above a critical surface density (Σ_{crit}) can incorporate more than $\sim$ 50% of the enriched gas into stars. In our suite the maximum recorded efficiency was $\sim$ 75%, attained in a Σ_{crit} "boosted" GMC run.

First we have to make sure that the variations of mean stellar surface density are caused by the contingency due to the insufficient sampling of binaries. We did a bootstrap to resample the binaries of each simulations with a given total system number, the results shown in Fig. **??** prove that the $\langle[\mathrm{Na/Fe}]\rangle_\star$ discrepancies among GMCs are not merely caused by the random formation of contamination sources. The right panel implies that the sub-populations might be an important factor to the [Na/Fe], which is similar to a so-called "Multi-Generational Cumulative Enrichment" proposed in Jenny J. Kim & Lee (2018). Given that knowledge, the formation of the first batch of enriched stars is getting more important, that's to say, the mixing process in a very early time is important.

6. KEY DRIVERS OF MULTIPLE POPULATIONS FORMATION

6.1. *Mixing Process*

In previous literature(Bastian et al. 2013), MP or its mass budget is calculated over a averaged level,i.e. comparing the total amount of 2P material to the pristine gas, as well as counting the ratio of 2P stars. However, although our simulations suffer from mass budget problem like many other simulations did, it's important to know how 2P gas released, enters, mixed and stayed within cold dense clump and eventually form the stars. In this section, we studied the impact of mixing process.

In order to confirm the existence of the effect of mixing, we develop a analytical model with assumption of instantaneous homogeneous chemical mixing, so that the [Na/Fe] variation is modulated by the star formation histories(See Sec.B). We adopt the M_{gas} and $M_\star$ by calculating the gas retains and the stellar mass within Lagrangian radius from the center of the newly born star clusters, and calculated population-average enrichment fraction from the yield table to model the Na mass fraction evolution with the infant star clusters, no enriched gas outflow is assumed, and eventually we derive the [Na/Fe] range of the model which is marked as the error bars and dash lines in Fig.10 and Fig.9. The maximum stellar [Na/Fe] of all our simulation have reached an order of [Na/Fe] $\sim$ 0.8, except for the most diffuse one(M1e6R100L0E1). The range of [Na/Fe](max minus min) of simulation is larger than what instantaneous mixing model predicted by a factor of $\sim$ 10, the magnitude is even more severe for more diffuse and yield boosted GMCs, up to 100 times wider [Na/Fe] range. which provides a proof for the existence of spatially and temporally inhomogeneous mixing.

In the rest of this section, we are going to present some metrics that are able to quantinize the inhomogeneous mixing within the proto-clusters during star formation and its relation to the mean stellar Na abundance.

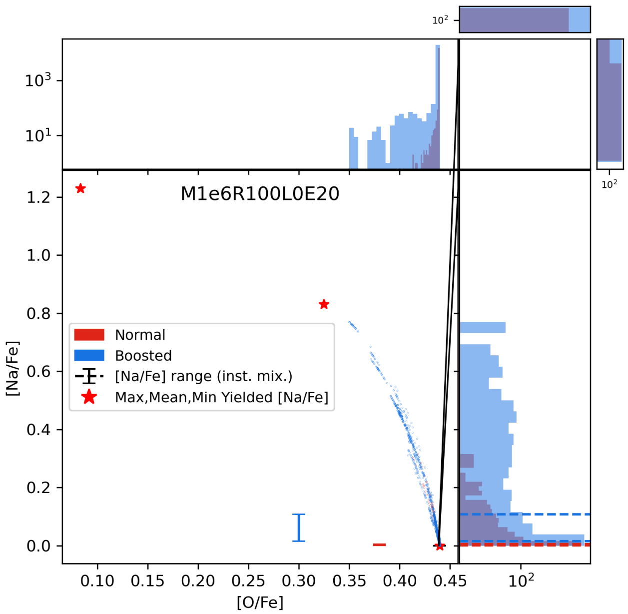

Figure 9. Na–O abundance distribution for simulation M1e6R100. Symbols/colors indicate the baseline enrichment scenario and boosted runs (blue: original yields; red: yields boosted by factor 20); red stars mark the maximum, mean and minimum yields from the yield tables. The distribution is dominated by a 1P locus with an extended 2P tail, illustrating spatially and temporally inhomogeneous enrichment.

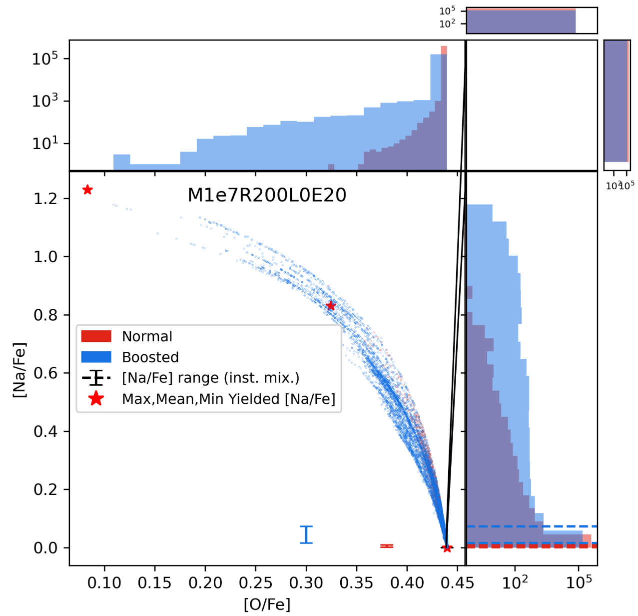

Figure 10. Na–O abundance distribution for simulation M1e7R200. As in the companion panel, blue points denote the original enrichment scenario and red points the boosted-yield case; annotations indicate yield-model extrema. The plot shows a dominant 1P population and an extended enriched tail rather than a single smooth locus.

6.2. *Gas evaporation on phase diagram*

To further investigate the inhomogeneous mixing evidenced by the enhanced [Na/Fe] spread, we analyze the diffusion of enriched gas using phase diagrams. This approach allows us to visualize how gas phases evolve during star formation and interact with enrichment sources. We begin by defining the key gas phases and the criteria for star formation. Closely following Deng et al. (2024), we adopt a temperature-based partitioning of the ISM into the following phases: cold neutral medium (CNM), defined as T < 100 K with an extra density selection $n > 10^4$ cm^{-3} introduced to preferentially select star-forming sub-structures; warm neutral medium (WNM), 100 K< T < 8000 K; warm ionized medium (WIM), 8000 K< T < 10 000 K; and hot ionized medium (HIM), T > 10 000 K. For the purposes of star-formation modeling, star-forming gas refers to a subset of CNM cells that additionally satisfy criteria for high density, gravitational boundedness (self-gravitating) and converging flows. it is expected to be converted into star particles on the local free-fall timescale $\sim \Delta t/t_{\rm ff}$ in RIGEL code.

Figure 11 displays the Na mass increment(final-initial) weighted phase diagram of gas, with the left, middle, and right columns corresponding to simulations at 10%, 50%, and 90% mass assembly epochs (i.e., t_{10}, t_{50}, t_{90}), respectively. Initially, MIB releases enriched gas into adjacent regions, where it rapidly mixes with cold, dense gas(”CNM” region in Fig. 11). A portion of this enriched gas is then heated and ionized by stellar feedback, leading to the appearance of enrichment signals in the 10^4 K regions on the phase diagram. The transition between the cold neutral medium (CNM) and the radiation ionized zone($T \sim 10^4$K) illustrates the dominant pathway for pollutants to escape star-forming regions: Pollutants preferentially enrich the densest CNM(this may due to our the zero yielding timescale setting), for the diffuse GMCs($\Sigma_0 < \Sigma_{\rm crit}$, the upper row in Figure 11), the enriched gas tend to escape from CNM zone along an isobaric track ($T \propto n^{-1}$), where the gas could keep thermal equilibrium, while for the dense GMCs($\Sigma_0 > \Sigma_{\rm crit}$, see the lower row in Figure 11), the enriched gas tend to evaporate without significant expansion.

Figure 12 shows the ratio of Na increment fraction of Isobaric track zone to that of ionization trap zone. The solid lines are the simulations with zero yield lag, unity yield boost factor color-coded by their initial surface density in unit

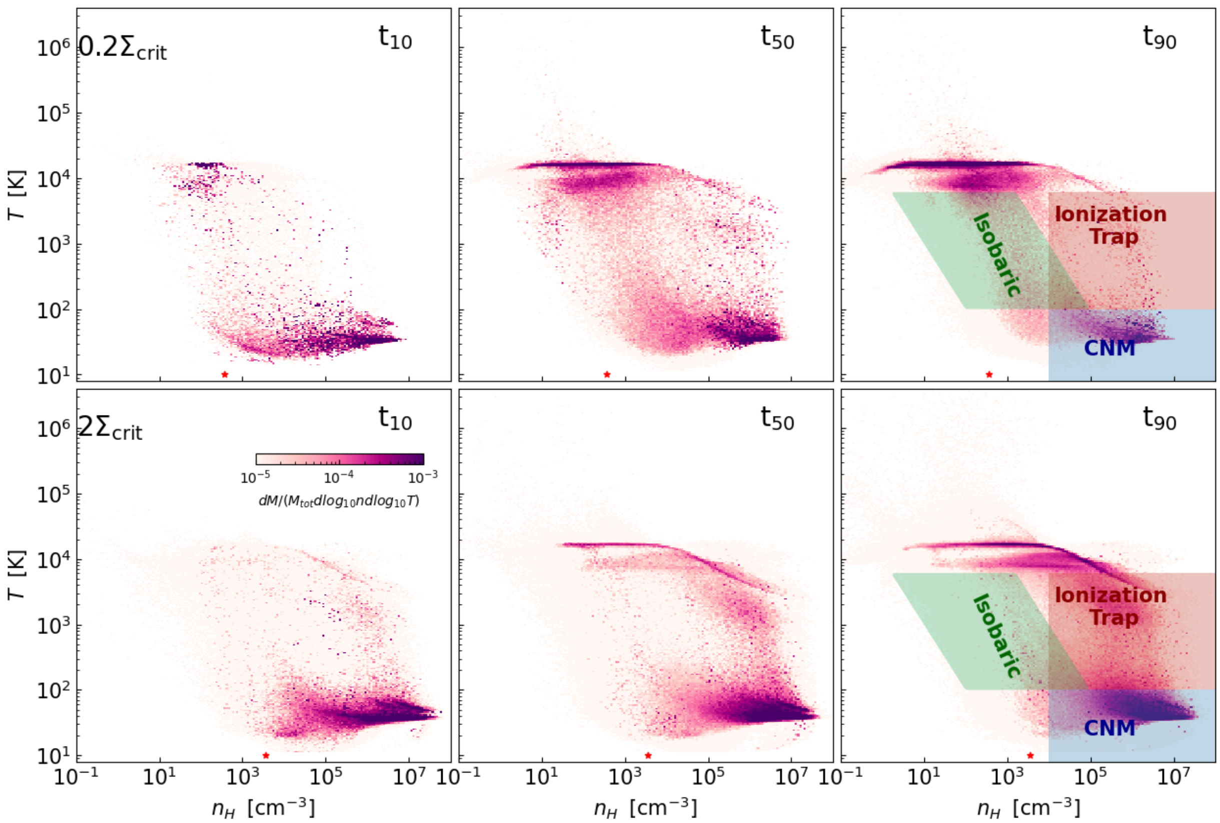

Figure 11. Na mass-increment (final − initial) weighted phase diagrams of the gas. Columns show three assembly epochs (t_{10}, t_{50}, t_{90}); rows compare diffuse ($\Sigma_0 < \Sigma_{\rm crit}$, upper row) and dense ($\Sigma_0 > \Sigma_{\rm crit}$, lower row) GMCs. Color indicates Na mass increment per phase bin; the diagrams trace the motion of enriched gas from cold, dense CNM into warmer/ionized phases. For diffuse clouds enriched gas tends to escape along an approximately isobaric track ($T \propto n^{-1}$), while for dense clouds enrichment is more confined and shows direct ionization trapping.

of $\Sigma_{\rm crit}$, the short dash lines in the right end of the figure are their time-averaged values. the mass ratio of enriched gas escape through isobaric track to that through gravitation bounded zone decrease as the increasing GMCs' initial surface density. This suggests that when the GMC is gravitation-dominated, the CNM gas being heated in a nearly isovolume manner and evaporate from the star-forming regions, while the CNM in the more diffuse giant molecular clouds escapes along a path of thermal equilibrium. No significant discrepancy between dash and solid lines with the same color proves that yield boost factor does not play an important role in changing the thermodynamic of the enriched gas. We also plot a pairs of simulations to illustrate the influence of yielding timescale on the phase diagram weighted by Na enrichment("M1e15L0E20" in thick solid line vs. "M1e5R15LNE20" in dotted line). The earlier the enrichment occurs, the more the enriched gas tends to be injected into the cold, dense phases of the interstellar medium (ISM), thereby leading to a higher 2P star formation.

Do the evaporation rates of these two channels differ? If so, could they contribute to 2P formation? To address this question, we first calculate the net heating timescale, defined as the difference between the thermal energy per H and its upper thermal limit($\rm T > T_{up,CNM} = 100$ K), divided by the net heating rate per H atom:

$$t_{\rm cool} = \frac{k_{\rm B}{\rm T}_{\rm up,CNM} - \langle U \rangle}{\langle \Lambda_{\rm net} \rangle}, \quad \langle U \rangle = \frac{\sum_i U_i}{\sum_i n_i V_i}, \quad \langle \Lambda_{\rm net} \rangle = \frac{\sum_i n_i^2 \Lambda_{net} V_i}{\sum_i n_i V_i} \tag{14}$$

where subscript i denotes i-th CNM particle, n_i is its number density, V_i its volume, $\Lambda_{\rm net}$ the net cooling rate, and U the thermal energy. This metric represents the time required for CNM to leave the star-forming region due to heating[2].

[2] Note that in all our simulation samples, the CNM during the star-forming phase is, on average, in a state of net heating, i.e. $\Lambda_{\rm net} > 0$. Therefore, using $k_{\rm B}{\rm T}_{\rm up,CNM} - \langle U \rangle$ as the numerator in the Eq.14 would be more reasonable, even though the notation is labeled as "cooling".

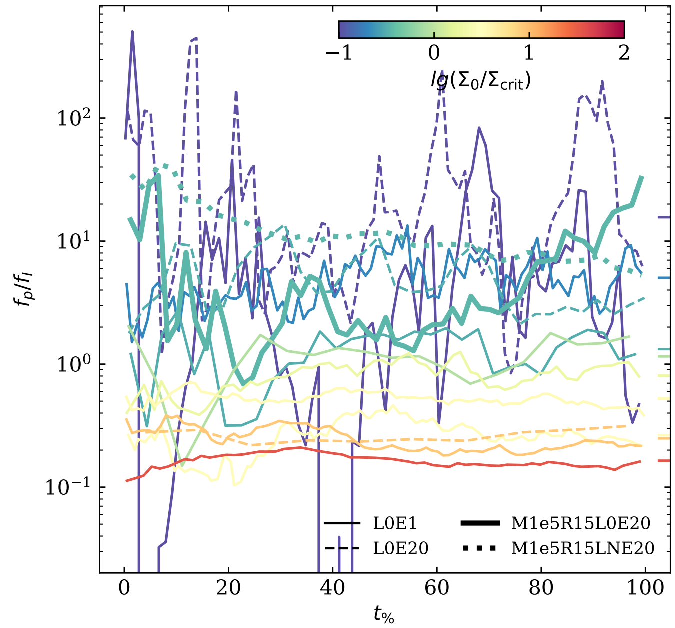

Figure 12. Ratio of Na increment fraction in the isobaric-track zone to that in the ionization-trap zone (f_p/f_i) as a function of time for selected simulations. Solid lines: zero-yield-lag, $\eta = 1$ runs color-coded by initial surface density normalized to Σ_{crit}; short-dashed lines at the right indicate time-averaged values. The mass ratio f_p/f_i decreases with increasing Σ_0, with a transition near $\Sigma_{\rm crit}$. Dotted/alternate curves illustrate the effect of different yielding timescales; earlier enrichment injects a larger fraction into cold, dense phases.

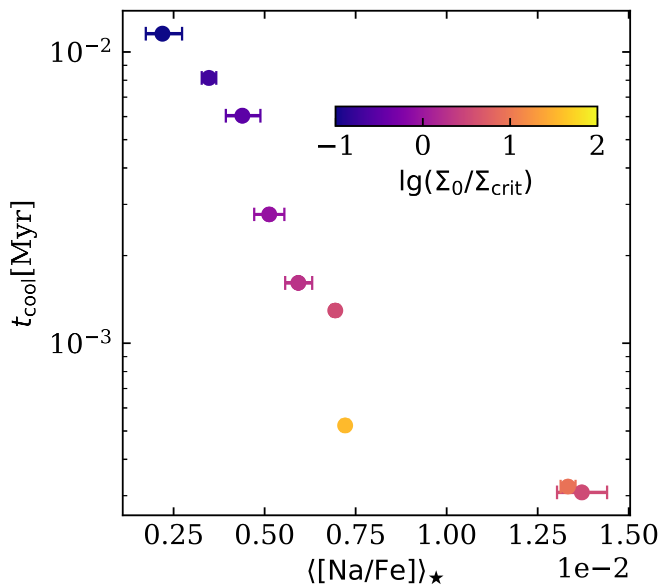

Figure 13. Net 'cooling' (heating) timescale t_{cool} (as defined in Eq. 14) versus mean stellar [Na/Fe] for all simulations; points are color-coded by initial surface density Σ_0. The plot shows a strong anti-correlation: shorter t_{cool} (faster net heating of CNM) is associated with higher mean stellar [Na/Fe], reflecting the role of gravitational confinement and turbulent energy partitioning in dense GMCs.

Figure 13 shows the net heating time versus mean stellar [Na/Fe], bullets are color-coded by Σ_0 of the GMC. We find a strong anti-correlation between the heating timescale and the mean stellar [Na/Fe]. Net heating rate represents the extent of the non-equilibrium of CNM, and this deviation could enhance the turbulent dissipation(Khurshid & Donzis 2019). This result seems contradict to our expectation, Conventionally, a shorter heating timescale implies that enriched gas is rapidly heated and expelled from the CNM phase before it can be incorporated into new stars. One would expect this rapid removal to suppress the capture of pollutants, resulting in lower stellar chemical enrichment. However, this apparent contradiction can be resolved by examining the energy budget under different gravitational potentials. As previously discussed, the shorter heating timescales are predominantly found in the most dense GMCs (e.g., $\Sigma_0 \sim 10^3\,{\rm M_\odot/pc^2}$). In these environments, the deep gravitational potential fundamentally alters the partition of feedback energy. Figure 14 reveals that in denser GMCs, a larger fraction of the injected energy is channeled into turbulent kinetic energy rather than thermal energy. Specifically, we observe that the ratio of turbulent to thermal energy rises steadily over time, and the time-averaged thermal-to-kinetic energy ratio remains significantly lower in dense GMCs compared to their diffuse counterparts. This suggests that in high-Σ environments, gravitational confinement prevents the rapid hydrodynamic expansion of heated gas, forcing a larger fraction of the feedback energy to drive a stronger turbulent cascade. Consequently, the turbulent mixing timescale becomes sufficiently short relative to the gas removal timescale(Hu 2025). The high [Na/Fe] abundance in these models serves as evidence that turbulent diffusion—which efficiently transports pollutants into star-forming cores—dominates over the suppression effect caused by thermal evaporation from the CNM.

6.3. *Spatial transport*

To track how fast the enriched gas transfer to and mix in the CNM region, we calculate the average over all stars of the mean distance from each star to its 32 nearest star-forming gas cells, $\langle L_{32}\rangle(t)$. This metric naturally reflects both the effective radius of the larger bubble between the stellar wind and the radiation, and indicates the average distance

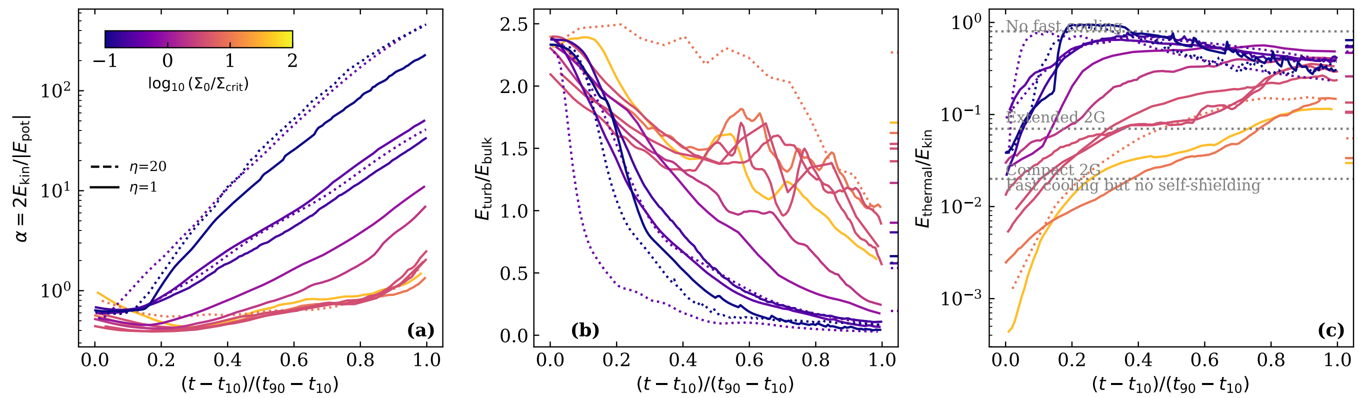

Figure 14. Energy partition between turbulent kinetic and thermal energy in the gas. Panels/curves (color-coded by Σ_0 or time) show that denser GMCs channel a larger fraction of injected feedback energy into turbulent motions rather than thermal energy; this elevated turbulent/thermal ratio enhances turbulent mixing and promotes the retention of pollutants in star-forming cores, helping explain the higher [Na/Fe] observed in dense runs.

from the contamination sources to the star-forming region. Figure 15 shows the temporal evolution of $\langle L_{32}\rangle$. The gray dash scaling are the effectively cooled(EC) wind bubble($\propto t^{(d+2)/(4-k_\rho)}$, Lachlan Lancaster et al. 2021; Lancaster et al. 2021b), respectively. The power law index of injected energy and density profile d and k_ρ are adopted from the measured parameters of our simulation, where $d \approx 2$ according to star formation history and $k_\rho = 0.8 - 2$ according to Fig. 6. In the early stages, the expansion rate of $\langle L_{32}\rangle$ is consistent with the theoretical expansion rate of stellar wind bubbles. However, in the later stages of star formation, the expansion of $\langle L_{32}\rangle$ in GMCs with lower Σ_0 becomes faster than theoretical predictions. This discrepancy may be attributed to the overall expansion of the giant molecular cloud itself, as this phenomenon is not observed in clouds with higher Σ_0. The $\langle L_{32}\rangle$ relative to initial radii R_0 generally decreases with increasing surface density, likely due to the higher ambient density slowing down the expansion of the bubble(Shown by the colors trend in Fig. 15). However, in the two GMCs with the highest Σ_0, the value of $\langle L_{32}\rangle$ sharply leap, deviating from this trend. This suggests that within GMCs at such high surface densities, the stellar density exceeds a critical threshold, leading to the merging of individual bubbles. We define a transport timescale to represent the time required for 2P ejecta to spread and reach the cold dense gas region:

$$\tau_{\mathrm{trans}}(t) = \frac{\langle L_{32}\rangle(t)}{v_{\mathrm{rms}}(t)} \tag{15}$$

, where v_{rms} is the density-weighted root mean square velocity. As is shown in Fig.16, we find that the time-averaged transport timescale is anti-correlated with the mean stellar [Na/Fe], and for GMC with $\Sigma_0 > \Sigma_{\mathrm{crit}}$, the correlation becomes weaker. This indicates that the shorter the time required for pollutants to propagate into CNM, the more favorable it is for MP formation. Thus, we have known that MP formation does not only depend on the quantity of chemical yield. Instead, it is jointly determined by the coupling between the thermodynamics of the interstellar medium during star formation, the distribution and cycling of energy, and the bubble dynamics. In summary, if Σ_0 is sufficiently high($\gtrsim 10^3 \mathrm{M_\odot pc^{-2}}$), WNM bubbles of individual stars might merge, which increase the average distance between pollution sources and the cold, dense gas within the cloud, thereby prolonging the time required for pollutants to be transported to the star-forming regions. Our results show a significant anti-correlation between this transport timescale and the mean stellar [Na/Fe]. When the Σ_0 exceeds Σ_{crit}, the gravitational potential well strongly suppresses the feedback-driven expansion of the gas (see Figure 11), leading to a larger fraction of turbulent kinetic energy (see Figures 14). These energy would cascade from forcing length scale to dissipation length scale and finally turn into thermal energy. However, the enhanced turbulent heating process also feeds the mixing and diffusion of 2P ejecta along the turbulent cascade(Liubin Pan & Scannapieco 2010). If, during this process, turbulent dissipation raises its temperature beyond the threshold for star-forming phases, this portion of enriched material will detach from the cold, dense star-forming gas and fail to be incorporated into next generation of stars. Our finding confirm that the cascade-driven diffusion is the winner effect of this competition: the mean stellar [Na/Fe] positively correlates with the net heating timescale per H of CNM gas.

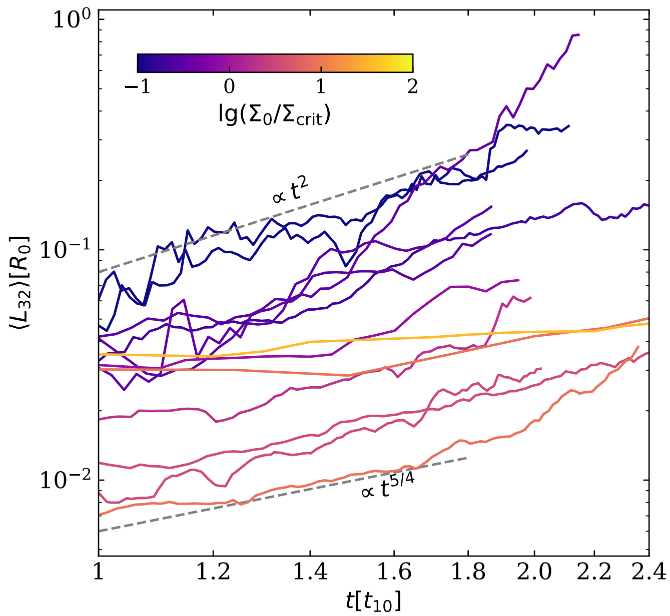

Figure 15. Temporal evolution of the average over all stars of the mean distance from each star to its 32 nearest star-forming gas cells, $\langle L_{32}\rangle(t)$, color-coded by initial surface density. The gray dash lines show the efficiently cooled stellar wind bubbles expansion law $R \propto t^{\frac{d+2}{4-\kappa}}$ (See Krause 2003; Lancaster et al. 2021b), with energy injection ($E(t) \propto t^2$) and power laws for density $\rho \propto r^{-\kappa}$, where $\kappa = 2$ and $\kappa = 0.8$ are the maximum and minimum power index of gas density radial profiles(Fig.6), respectively.

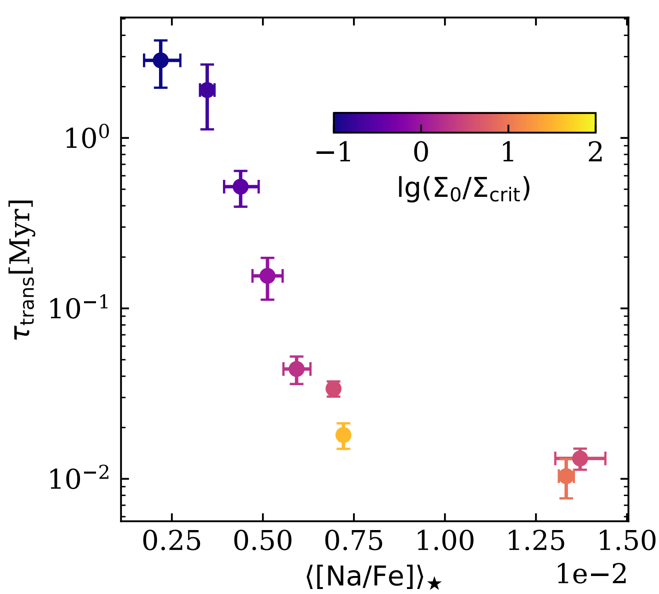

Figure 16. Transport timescale(Eq.15) as a function of Mean stellar [Na/Fe]. The circles with error bar are color coded by the initial surface density of each simulation.

In the next section we will focus on quantifying the spatial and temporal scales of enriched gas diffusion within cold, dense gas—including measurements of the turbulent diffusion coefficient, dissipation timescale, and mass flux—to further determine which mechanism truly dominates the formation or absence of 2P stars under different Σ_0 conditions.

6.4. *Mixing Timescales*

In the above section, we utilize phase diagram, energy partition, bubble dynamics, and related parameters to quantify how, and at what rate, could enriched gas transport from contamination sources to star-forming regions and finally be evaporated, but the coupling between star formation and the turbulent mixing of enriched gas also significantly influences the MP formation. In idealized scalar mixing experiments, contaminants are typically released either from a single source or are assumed to have a uniform abundance. However, in our simulations, the chemical yield is somehow stochastic, defining a baseline for mixing(i.e. an abundance representing pure pollutant) is really problematic, due to its dependence on not only the IMF but also the yield model employed. Therefore, we use the primordial fraction P as the tracer of mixing, which is defined by the mass fraction of the gas whose $[\mathrm{Na/Fe}] - [\mathrm{Na/Fe}]_{\mathrm{init}} < 0.0002$. Then the time evolution of primordial fraction of ISM can be described as

$$\frac{dP}{dt} = -\frac{1}{\tau_{\mathrm{mix}}} P(1-P) - \frac{1}{\tau_{\mathrm{src}}} P + \frac{1}{\tau_{\mathrm{sf}}} (P - P_s) \tag{16}$$

where τ_{mix} is the time required for all the tracer elements to be stretched into sheets and to experience interactions; τ_{src} is a characteristic time for primordial gas passed through stars that became the enriched ejecta; τ_{sf} is the time require for primordial gas incorporate into the stars, since the yield lag in our work is zero, we have $\tau_{\mathrm{sf}} = \frac{\tau_{\mathrm{src}}}{f_{\mathrm{y}}\eta}$,$f_{\mathrm{y}} = 0.0345$ is the IMF-averaged returned fraction(Total Ejected mass over Total stellar mass) from polluters, η is the boost factor of chemical yield(see Section 3 for details); P_s is the primordial fraction of stars. For low-Σ_0 GMCs, chemical mixing appears to be localized. the primordial fraction of stars P_s often rebounds during the star formation period, sometimes even returning close to 1 in the late stages. In contrast, for high-Σ_0 GMCs, P_s gradually decreases during star formation, and the higher Σ_0, the earlier P_s approaches zero. Fig.18(c) shows the time-averaged P_s as a function of Σ_0, as well as the fitted curve using the equation as follow:

$$P_s = \frac{1}{2} - \frac{1}{\pi} \arctan\left(\lg\left(\frac{\Sigma_0}{\mathrm{M_\odot/pc^2}}\right) - 2.41\right) \tag{17}$$

. Inserting this formula into our model and solving Eq. 16 yields

$$P(t) = \sqrt{k}\frac{1 + C_0 e^{2A\sqrt{k}t}}{1 - C_0 e^{2A\sqrt{k}t}} - \frac{B}{2A} \tag{18}$$

,where $A = \frac{1}{\tau_{\mathrm{mix}}}, B = \frac{f_{\mathrm{y}}\eta - 1}{\tau_{\mathrm{src}}} - \frac{1}{\tau_{\mathrm{mix}}}, C = -\frac{f_{\mathrm{y}}\eta}{\tau_{\mathrm{src}}} P_s, k = \frac{B^2 - 4AC}{4A^2}, C_0 = \frac{P_0 - \sqrt{k} + \frac{B}{2A}}{P_0 + \sqrt{k} + \frac{B}{2A}}$, and $P_0 \approx 1$ is the primordial fraction at $t = 0$. In this model, the mixing rate is proportional to $P(1-P)$, which implicitly assumes that the effective interaction area between the unpolluted and unpolluted regions is proportional to the product of their respective mass fractions, this assumption holds only when the pollutants have not yet been sufficiently stretched and dispersed(Liubin Pan ????; Pan et al. 2012). In addition, primordial fraction could no longer serve as a reliable proxy indicator for turbulent mixing processes when it is small. Therefore, we use Eq. 18 to fit the primordial fraction in the period from 1% to 70% stellar mass assembly epoch(i.e. t_{01}, t_{70}), which ensure all the P is larger than ~ 0.5(Figure 17).

Figure 18(a) and (b) show the fitted source timescale and mixing timescale as the function of initial surface density Σ_0, respectively. As shown in Figure 18(a) and (b), we find that both the mixing timescale and the source timescale exhibit linear scaling laws with the initial surface density. The gray lines in these figures are

$$\lg\left(\frac{\tau_{\mathrm{mix}}}{\mathrm{Myr}}\right) = -0.42 \lg\left(\frac{\Sigma_0}{\mathrm{M_\odot/pc^2}}\right) + 1.01 \tag{19}$$

$$\lg\left(\frac{\tau_{\mathrm{src}}}{\mathrm{Myr}}\right) = -1.09 \lg\left(\frac{\Sigma_0}{\mathrm{M_\odot/pc^2}}\right) + 4.27 \tag{20}$$

,respectively. . a surface-density-independent relation $\tau_{mix} \approx 0.3\langle\tau_c\rangle_t$ is also found(See Figure 18), where $\langle\tau_c\rangle_t$ is the time-average concentration dissipation timescale, which is used to capture the linear extent of the region within scalars are appreciably correlated(Pan 2008; Liubin Pan & Scannapieco 2010; Batchelor, George Keith. 1953)

$$R_X(r) = \langle X(x)X(x+r)\rangle, \quad L_X \equiv \frac{\int R_X(r)dr}{R_X(0)}, \quad \tau_c \equiv \frac{L_c^{2/3} L_v^{1/3}}{v_t} \tag{21}$$

, where X is a passive scalar field, in Eq.21 it is $X = c$ for concentration and $X = v$ for velocity, $R_X(r)$ is the two-point

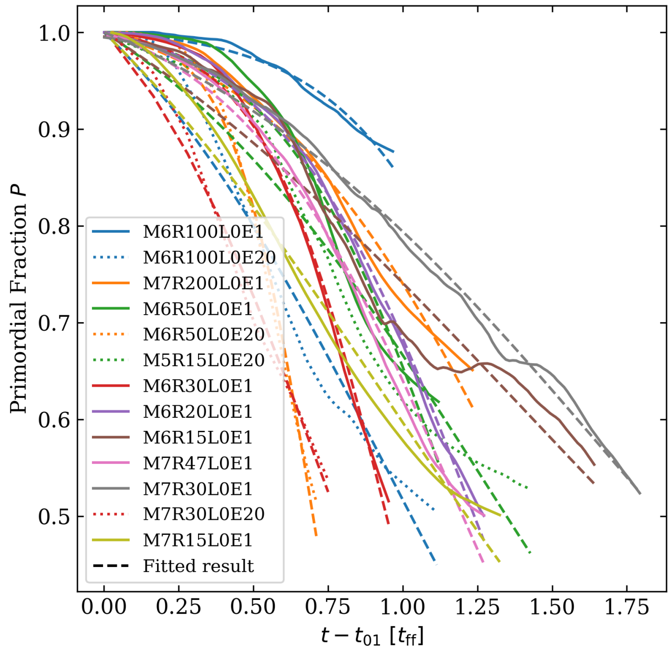

Figure 17. Primordial fraction as a function of the time since first 1% stellar mass assembly(t_{01}). Solid lines are the primordial fraction of the simulations with yield boost factor $\eta = 1$, dotted lines are the simulations with $\eta = 20$. Dashed lines show the best fitted result of Eq.16.

correlation function of the scalar field, L_X is the scalar correlation length of the corresponding scalar field, v_t is the turbulent velocity scale, here we use tangential velocity to represent it, in order to avoid the contamination by bulk motion of the flow. This metric represents the time needed for the concentration cascading into a smaller characteristic length scale. That scaling relation is similar to the measurement made in theoretical models(e.g. Janicka et al. 1979; Curl 1963). Liubin Pan (????) provides a simple estimation of source timescale, which is

$$\tau_{src} = \frac{M_g}{\eta \mathrm{sfr} f_{\mathrm{y}}} \approx \frac{1-\varepsilon_{int}}{f_{\mathrm{y}} \eta \varepsilon_{int}} \frac{\tau_{\mathrm{dur}}}{2} \tag{22}$$

, where $\mathrm{sfr} = 2M_*/\tau_{\mathrm{dur}}$ is the equivalent uniform star formation rate under the assumption of triangle star formation history(Eq.B2). Inserting values of ε_{int} and τ_{dur} predicted by Li et al. (2019) to Eq.22, we get the theoretical source timescales shown in open circles and squares in Fig.18, which are broadly consistent with our measurements. Now both τ_{src} and τ_{mix} are expressed as the parameter which is either calculable from one snapshot, By defining a primordial fraction P', such that the mean [Na/Fe] of the gas which has been involved in mixing (i.e. non-primordial gas) equals 2P threshold([Na/Fe]>0.3 in our work), we can derive a 2P maintenance timeτ_{2P}, which is

$$P' = P(\tau_{2P}) = 1 - M_{\mathrm{y}}\left(1 + \frac{kX_{\mathrm{Fe}} - X_{\mathrm{Na}}}{X_{\mathrm{init,Na}} - kX_{\mathrm{init,Fe}}}\right), k = 10^{[\mathrm{Na/Fe}]_{\mathrm{thres}} m_{\mathrm{Na}}/m_{\mathrm{Fe}}} \tag{23}$$

. Figure 19 shows the 2P maintenance time per star formation duration as a function of initial surface density. We find that although τ_{2P} decrease with increasing Σ_0, their value relative to star formation duration time split into two distinct sequences with different total mass of GMCs, as shown in Fig.19, M1e6 $\tau_{\mathrm{2P}}(\Sigma_0)/t_{\mathrm{dur}}(\Sigma_0)$ curve(red line) is higher and peak at lower Σ_0 than M1e7 sequence(blue line), The cross markers denote the cumulative sum of the durations during which the 2P mass increment exceeds 1% of the total 2P stellar mass. The close agreement between τ_{2P} and this directly measured 2P-active time proves that this timescale is a physically meaningful and robust measure of the effective 2P star formation window across different GMC masses and initial surface density.

6.5. *Optimal GMC parameter space*

Heatmap of $\tau_{\mathrm{2P}}/t_{\mathrm{dur}}$ in the GMC (M, R) plane is shown as gray shaded region in Fig. 20, while other labels are the same as Fig.7. Our simulations indicate that the parameter space maximizing $\tau_{\mathrm{2P}}/t_{\mathrm{dur}}$ lies at GMC surface densities

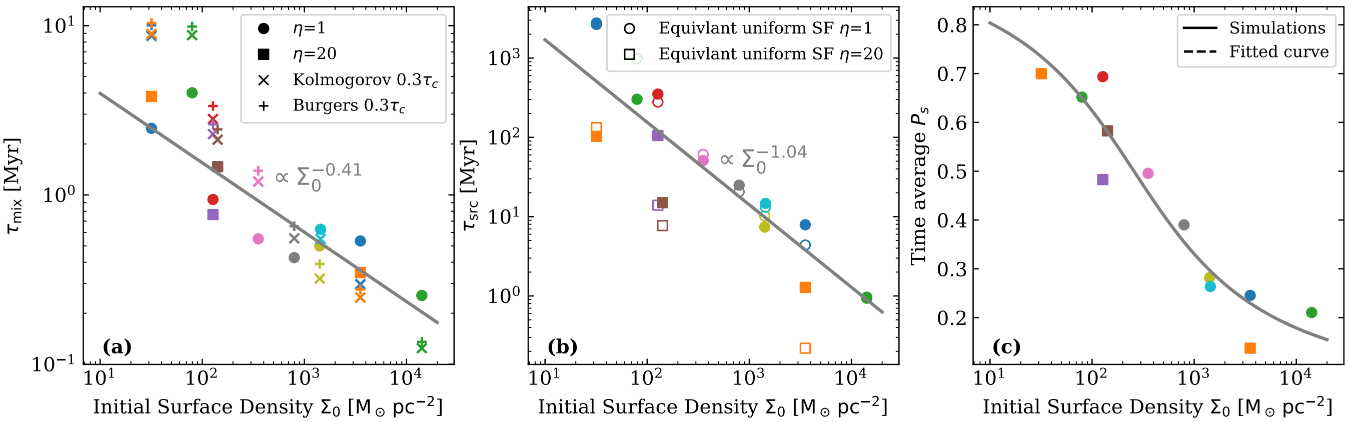

Figure 18. Mixing timescale($\tau_{\rm mix}$, panel (a)), source timescale($\tau_{\rm src}$, panel (b)) and Time-Averaged primordial star fraction(P_s,panel (c)) as a function of initial surface densityΣ_0. Filled markers of all panels are the fitted values to 13 zero yield lag simulations(See Table 1), shapes of whom distinguish different yield boost η, circles for $\eta = 1$, and squares for $\eta = 20$. Gray curves are the best-fit results of Eq.19, Eq.20,Eq.17, respectively. Panel (a): cross mark and plus mark denote the concentration dissipation timescale under the assumption of Kolmogorov's and Burger's inertial-range scaling, respectively. Panel (b): Open marks show the estimated source scale using Eq.22, the shapes of whom distinguish different yield boost η, circles for $\eta = 1$, and squares for $\eta = 20$, respectively.

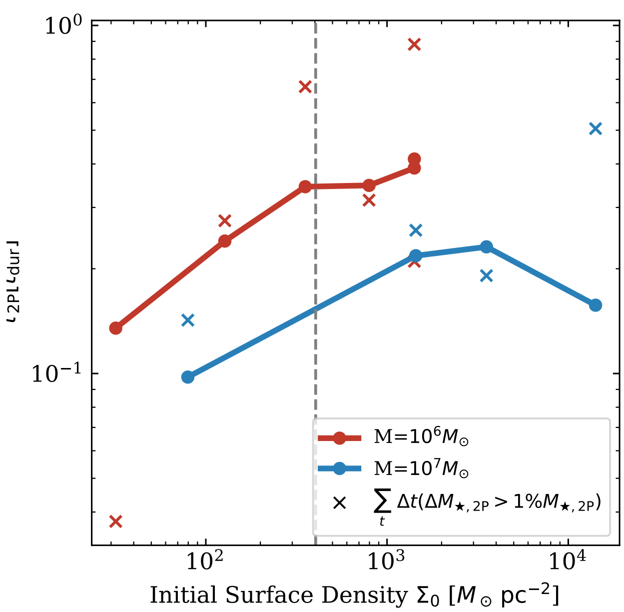

Figure 19. Second population maintenance timescale per star formation duration as a function of initial surface density. Red and blue color show the data from the simulation with initial mass M = $10^6 M_\odot$, and M = $10^7 M_\odot$, respectively, solid lines show the second population maintenance timescale calculated using primordial fraction evolution(Eq.23), divided by star formation duration($t_{\rm dur} = t_{90} - t_{10}$). Cross marks show the total duration during which the growth rate of the 2P fraction exceeds 1% of the final 2P fraction, this metric could be regarded as "real" 2P maintenance timescale, which directly measure the duration of high 2P growth rate.

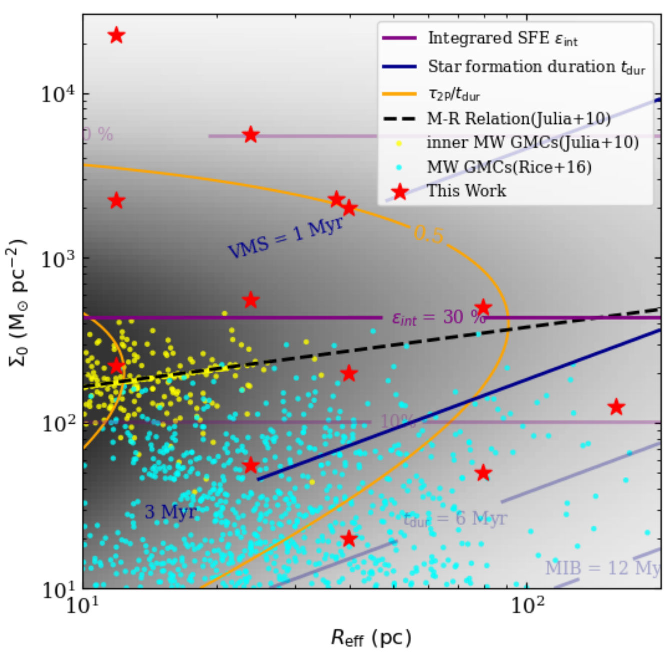

Figure 20. GMC's surface density versus initial radius parameter space. Labels in this figure are the same as Fig.7, black dash line denotes the M-R relation of inner MW GMCs(Eq.13 in Julia Roman-Duval et al. 2010), Gray shaded contour shows the heat map of 2P maintenance timescale, deeper color represents larger τ_{2P}. Optimal parameter space of 2P formation is larger than MW GMCs in surface density axis, which might account for the extinction of multiple populations in present-day star clusters.

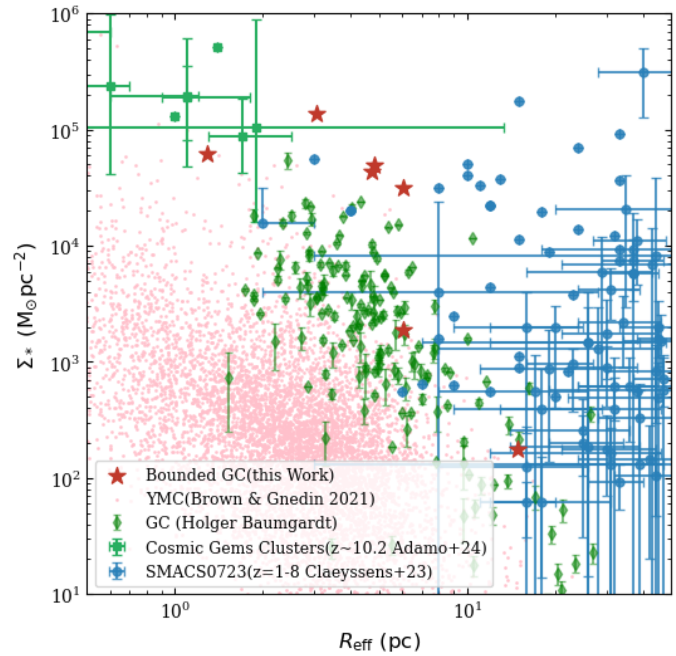

Figure 21. Stellar cluster's surface density versus half mass radius(effective radius) parameter space. Red stars show the bounded GC obtained in this work, Green diamonds: Globular clusters in Holger Baumgardt's GC catalog. Pink dots: YSC from in 31 galaxies from the Legacy Extragalactic UV Survey(LEGUS, Brown & Gnedin 2021). Blue circles: stellar clumps in 18 lensed galaxies at redshifts 1–8.5 within the lensing cluster field SMACS0723(Claeyssens et al. 2023). Green circles: Star clusters in The Cosmic Gems arc at redshift ∼ 10.2 (Adamo et al. 2024).

systematically higher than those characteristic of Milky Way GMCs(cyan dots from Rice et al. 2016), but are closer to those of inner milky way GMCs(See yellow dots and black-dash lines provided by Julia Roman-Duval et al. 2010). This suggests that present-day Milky Way GMCs may not occupy the parameter space most favorable to 2P formation. As shown in Fig.21, bounded star clusters obtained in our work are similar to Holger Baumgardt's GC catalog[3] in surface density and half mass radius. Interestingly, high-z globular cluster precursors are inferred to be both more massive and denser (and in some cases larger) than young massive clusters in the local Universe, assuming that MW GMCs are the progenitors of present-day YMCs, then the high-z star clusters, which generally exhibit greater masses than YMCs(See Fig.21), may have originated from even larger and denser GMCs. It is plausible that such GMCs would occupy parameter spaces more closely aligned with the optimal 2P formation parameter space in Fig.20. This alignment may well imply that our results offers a natural explanation for why MP are only observed in ancient globular clusters, but not in the local Universe.

7. DISCUSSION

Through star formation simulations, we explored the key drivers of the multiple populations formation. We now compare our results with the relevant literature and discuss the strengths and limits of our approach.

7.1. *Implications for MP formation*

The mass budget problem remains one of the most significant challenges in explaining the MP formation in globular clusters for multiple generation scenarios. Even the massive interacting binary(MIB, De Mink et al. 2009; Michelle

[3] https://people.smp.uq.edu.au/HolgerBaumgardt/globular/parameter.html

Nguyen & Sills 2024) model employed in our work, still struggles with the mass budget problem, as many other similar models do. In our simulations, even when the ejected mass is increased by a factor of 20($\eta = 20$, equilvalent to $\sim$ 60% of the mass of every binary) and assuming that stars release all pollutants immediately upon formation(yield lag L=0), 2P fraction is only up to $\sim 6\%$. This result aligns with the calculations of Bastian & Lardo (2018) in extreme assumption, as well as the simulation results from Lahén et al. (2024); Vesperini et al. (2010). Obviously, the challenge posed by the mass budget to the multiple generations scenario originate from the limited total amount of enriched gas due to the nature of IMF. Enhancing the wind production by a top-heavy IMF as a solution was first proposed by Prantzos & Charbonnel (2006). Interestingly, top-heavy IMF is also necessary to explain the UV-luminous galaxies in early Universe(e.g. Jeong et al. 2024; Matzner 2024), Li et al. (2023) also confirm a correlation between IMF slope and the metallicity. These findings, to some extent, align with the requirements for the MP formation and also hint the origin of the exclusivity of this phenomenon in ancient globular clusters, compared to their absence in young star clusters in local Universe. Another direction of solution is high 1P mass loss by dynamical mechanisms. For example, tidal strips during their long-term evolution(Lacchin et al. 2024; D'Ercole et al. 2008), these mechanisms always require a highly central concentrated 2P distribution so that the stripped stars could be dominated by 1P stars(Milone et al. 2020). However, No significant discrepancy of spatial distribution between 2P and 1P stars is detected in our work, probably because the time interval between the release of enriched gas and its incorporation into the 2P stars is insufficient to allow for significant radial distribution changes in the 1P stars.

Despite insufficient total 2P fraction, the abundance distribution in our work exhibit more extensive abundance spread comparing to that of Lahén et al. (2024), which might account for shorter yielding timescale in our work. The long tail with discrete clumps and tracks are the signals of inhomogeneous mixed pollutant among star-forming clumps, which guarantee the relatively flatten distribution at most of non-pristine abundance range, as well as the steady abundance extrema in the infant globular clusters.

We also reveal a so-called "time budget" problem in isolated GMC: the conflict of high star formation efficiency versus high star formation duration(See Fig. 7 and Sec.5.1), the timing mismatch between pollutant release, turbulent mixing, and star formation duration also strongly limits the fraction of 2P stars(Sec. 6). About 90% percent of GMCs in MW-mass galaxies (Ni et al. 2025) would be disrupted because of stellar feedback within $\lesssim$ 10 Myr, which means for self-enrichment scenario, there is no chance for the stars more massive than $\sim 20\mathrm{M}_\odot$ to release their chemical yield promptly(Limongi & Chieffi 2018). This constrant, together with the observed strong nitrogen emission in some high-z objects make very massive stars(VMS, see e.g. Vink 2023) stand out. However, If consider the impact of environmental factors,such as cloud-cloud collision, gas inflow conditions(Fukui et al. 2020; Maity et al. 2024; Glen H Hunter et al. 2023; Wu et al. 2017, 2015), the SFD may be decoupled from SFE, thereby expanding the feasible parameter space for MP formation.

Our work indicates that the chemical abundance characteristics of MP (represented by mean stellar [Na/Fe]) are correlated with the initial surface density(Σ_0) of their progenitor GMCs. However, the underlying mechanism differs from the previous scenario in the literature, which suggested that deeper gravitational potential wells better retain enriched gas to form more 2P stars(e.g. Charlie & Spergel 2011). This earlier assumption typically posited that 2P gas is first expelled and then re-accreted into the cluster over an extended period, creating the impression that larger gravitational potentials retain more 2P gas and thus produce more 2P stars. In contrast, in our simulations, 2P stars formed prior to gas expulsion, with the star formation timescale in most GMCs being shorter than that of SNe, thereby avoiding contamination by supernova ejecta.

our realistic simulations reveal that MP are not proportional to the Σ_0 of GMCs. Instead, they correlate with the degree to which cold dense gas deviates from thermal equilibrium (characterized by the net heating rate, see Sec.6.2) and the timescale for pollutants to traverse hot bubbles and enter cold, dense gas (characterized by the crossing timescale, see Sec.6.3). As the surface density increases, gravitational pressure progressively suppresses the thermal expansion of enriched gas, resulting in an evaporation pathway on the phase diagram that approximates an isochoric process. Turbulence becomes more efficient at transferring energy to dissipative scales through the cascade process, thereby enhancing the diffusion rate of the enriched material it carries. However, once the surface density exceeds a critical threshold, the dense stellar field causes hot bubbles(Ionized or wind bubble) generated by stellar feedback to merge, significantly increasing the distance between polluters and star-forming regions. This lengthens the spatial transport timescale for pollutants, ultimately leading to a weakening of the resulting multiple stellar populations. The abundance initially increases with Σ_0 before declining until $\Sigma_0 \sim 10^3 - 10^4\mathrm{M}_\odot\mathrm{pc}^{-2}$, the turning point aligns closely with the critical surface density predicted in the literature, where star formation transitions from turbulence-dominated to radiation-dominated, and stellar feedback balances the self-gravity of the molecular cloud(Ostriker & Shetty 2011; Lancaster et al. 2021a; **?**). This suggests that the manifestation of MP is ultimately regulated by the interplay of gravitational collapse, stellar feedback, and turbulent mixing.

By tracking the temporal evolution of the primordial gas fraction, we have indirectly investigated the influence of turbulent mixing on the proportion of 2P gas in GMCs with varying initial surface densities(Sec.6.4). This indirect approach is adopted for mainly two reasons. First, under yield lag = 0 condition in this study, most 2P gas is rapidly incorporated into stars(See lower right panel in Fig.4), causing 2P gas fraction to fluctuate strongly over time. In contrast, the primordial gas fraction is more sensitive to turbulent mixing and remains unaffected by subsequent star formation and enrichment processes. Second, the statistical noise in the primordial gas fraction is relatively low, which facilitates the quantification of scale-dependent and temporal characteristics of mixing, whereas 2P abundances are susceptible to individual pollution events and small-sample statistical fluctuations. Therefore, within this research framework, the primordial gas fraction serves as a more reliable tracer of turbulent mixing.

From those perspectives, we assert that isolated giant molecular clouds cannot form multiple stellar populations with the polluters of massive stars constrained by a normal initial mass function. We suggest that a viable multiple-generation MP scenario must include (1) either fast, prompt polluters, or external mechanism that decouple SFE from SFD, (2) an efficient dynamical mechanism that removes $\sim 90\%$ of primordial stars so that the remaining population naturally yields the observed near-uniform or bimodal abundance patterns under inhomogeneous mixing; and (3) progenitor GMCs that sit in a "Goldilocks'' surface density (or equivalent external-pressure) regime, which is dense enough to suppress bubble expansion and drive turbulent mixing, but not so dense that bubble merging greatly lengthens pollutant transport times or prematurely truncates the 2P formation window. A MP formation scenario that include fast polluters, such as very massive stars(VMS,$\sim 10^2 M_\odot$, using definition from e.g. Vink 2023), super massive stars(SMS,$\sim 10^3 M_\odot$, Bastian & Lardo 2018), that could yield 2P gas with $\lesssim 3$ Myr, plus cloud-cloud collision model is going to be tested in our future work.

7.2. *Limitations and future perspectives*

We note that there are a few caveats and limitations of this work.

7.2.1. *Caveats on Binary yield model*

While our model provides a detailed accounting of the chemical budget from massive binaries, several simplifications regarding stellar dynamics and binary physics warrant discussion. We start by explaining the CCSNe mass range($8M_\odot - 40M_\odot$) of the stars. The upper bound of 40 $M_\odot$ is set by the onset of direct collapse into black holes in metal-poor massive stars (See similar implication from Xu et al. 2025; Heger et al. 2003), and the maximum mass in our model does not exceed the mass threshold for pulsational pair-instability(PPI, Heger & Woosley 2002). The lower boundary, however, remains somewhat ambiguous. For primaries with $M_1 \in [8, 10]M_\odot$, the helium cores (typically $\approx 2M_\odot$) lie close to or slightly below the empirical lower limits for the explodability of Type Ib/Ic supernovae($\gtrsim 12M_\odot$, e.g. Yoon et al. 2010; Yoon 2015), binary-stripped stars($\gtrsim 10M_\odot$, see Farmer et al. 2023; Vartanyan et al. 2021) and electron-capture supernovae (ECSN,$13.2M_\odot - 17.6M_\odot$ according to Poelarends et al. 2017). Their subsequent fate depends sensitively on the structure of the remaining core, such as density profile and compactness, which affect both explodability and explosion energy (Laplace et al. 2021; Vartanyan et al. 2021; Gutcke et al. 2021; Steinwandel & Goldberg 2025). Binary interaction will also cause SNe feedback delayed and displace (Wagg et al. 2025), their effect on star formation and MP formation will be investigated in our upcoming work.We here omit impact of these marginal cases on the integrated feedback budget.

As previously mentioned, the binary stars in this study serve solely as sources of enrichment, and their corresponding dynamical entities are identical to those in RIGEL, which did not track the dynamics of the massive stars. Consequently, our model does not capture the effects of multi-body interactions on the feedback and enrichment of binary populations. Although existing literature has demonstrated that during cluster formation, massive binaries frequently undergo events such as companion exchange, dynamical capture, orbital hardening, and binary disruption due to multi-body interactions, these events do not significantly alter the binary fraction or the distribution of orbital parameters(Cournoyer-Cloutier et al. 2024). Therefore, we have neglected their effects, in this version of the binary enrichment model. In the upcoming RIGEL-2 or Arepo-N, we are going to implement corresponding improvements to this binary enrichment model to better replicate more general and realistic physical conditions. We didn't consider the effect of the rotation, which might contribute to both rejuvenation and chemical yield(De Mink et al. 2009), the secondary will reach its critical rotation after first time mass transfer, and the critical rotation will elongate its age by $\sim 40\%$ for massive stars(See figure 4 in Georgy et al. 2013). On the other hand, the chemical yield of this kind of secondary can smoothly switch to fast rotating stars model(e.g. Nandal et al. 2024). However, the spin of stars are highly related to the structure of both components and the timing of binary interactions starts and stops(see e.g. S. E. De Mink et al. 2013). We have not yet implemented such effect into our model.

7.2.2. *Caveats on chemical mixing model*

It should be noted that we don't, and find it hard to directly model the mixing process base on gas abundance probability density distribution(pdf) as many literature do(such as scalar variance, contaminant density in Ralf S. Klessen & Lin 2003; Liubin Pan & Scannapieco 2010; Colbrook et al. 2017), the mixing model employed in this study is an equivalent model with constant mixing–enrichment–star formation timescales, which is applicable to early stages when pollutants are sparse and still distributed in sheet-like structures. Once the concentration field is highly stretched and folded by turbulence into a fractal structure, the model's assumption that "the contact area is proportional to the pollutant fraction" no longer holds. Furthermore, the 2P maintenance timescale($\tau_{\rm 2P}$), defined based on primordial gas, essentially represents the time required for the overall abundance of gas participating in turbulent mixing and material cycling to fall below the 2P threshold. This definition implicitly assumes the simplified condition that "primordial gas becomes instantaneously and fully mixed once polluted"—only under this condition does this timescale strictly correspond to the cutoff time for 2P star formation. By comparing the instantaneous 2P star fraction, we find that this timescale generally aligns with the cumulative period during which the 2P stellar mass increment exceeds 1%. Moreover, its variation with the initial surface density of GMCs is fully consistent with the total duration over which the instantaneous 2P star fraction remains above its final value. Notably, in the M1e7 track, the latter duration is approximately 2.4 times longer than the former, the specific reasons for which warrant further investigation. Therefore, we propose that $\tau_{\rm 2P}/t_{\rm dur}$ be used as a reference indicator for the time window of MP formation, rather than as a precise quantitative estimate.

8. CONCLUSION

In this work, We implemented a self-consistent model of chemical enrichment from massive interacting binaries (MIBs), coupling binary population synthesis, time-dependent yields and the realistic ISM modeling. We incorporate observation-based probability distributions for binary parameters, MESA-based binary chemical yield table, mass transfer timescale criterion system, and a rejuvenation model to self-consistently track the star-to-star pre-SN evolution of binary stars across broad ranges of primary stars from $8-100$ $\rm M_\odot$, period from $10^{0.2-0.8}$ days, mass ratio from 0.1 to 1, while the parameter space of chemical yield is limited to that of the pre-calculated data(range of Case-B mass transfer, primary stars from $8-40$ $\rm M_\odot$, period from $2-700$ days). In this work, We performed a suite of high-resolution simulations of isolated GMCs spanning a wide range of masses, radii, and surface densities to investigate how the formation of multiple stellar populations (MPs) in young globular clusters is regulated by the initial conditions of their natal giant molecular clouds (GMCs). The degree of MP does not vary monotonically with the initial surface density, but is regulated by a coupled chain of "feedback–turbulence–mixing". The main findings of our work are summarized as follows:

1. Even under extreme setting that maximize enrichment capacity and temporal diffusion window, 2P mass ratio rarely exceed $\sim 6\%$, isolated GMCs cannot form multiple stellar populations with the polluters of massive stars constrained by a normal initial mass function. In zero yield lag case, the mass fraction of the enriched gas incorporated into stars is up to 40%, which is one order magnitude higher than that in normal cases.

2. Inhomogeneous chemical mixing allows stellar populations to produce an uniform distributions that similar to observations within the abundance range of pollutants. The maximum abundance dispersion in stars can reach several tens of times that of the uniformly mixed scenario. Some simulations with low initial surface densities exhibit a slight bimodal distribution, all of which result from the localized enrichment or inhomogeneous mixing of pollutants. The overall stellar abundance distribution consists of a uniformly enhanced abundance component plus a sharp spike of unenhanced abundance.

3. second-population fraction exhibits a strong, non-monotonic dependence on GMC initial conditions. Mean stellar [Na/Fe] peaks at $\Sigma_0 \sim 10^3 - 10^4$ $\rm M_\odot pc^{-2}$, close to the Eddington critical density of star formation(defined in Thompson & Krumholz 2016; Lancaster et al. 2021a). By analyzing the thermal equilibrium state of cold

neutral medium(CNM), we find that the mean stellar [Na/Fe] correlate with the net heating rate of the CNM, and anticorrelate with the transport timescale for pollutants to travel from stellar neighbor to the star-forming regions.

4. The turbulent mixing timescale during star formation deceases with increasing initial surface density, but the source timescale decreases more rapidly. Consequently, the trend of 2P maintenance timescale per star formation duration reverses near a critical initial surface density. This trend is associated with the non-monotonic variation of the second-generation fraction with respect to initial surface density.

5. Through 2P maintenance timescale per star formation duration, we derive the optimal GMC parameter space for MP formation, which are $10\ \mathrm{M_{\odot}pc^{-2}} \lesssim \Sigma_0 \lesssim 200\ \mathrm{M_{\odot}pc^{-2}}, 10\ \mathrm{pc} \lesssim R_0 \lesssim 30$ pc. We find it lies systematically at higher surface densities than those characteristic of present-day Milky Way GMCs. Based on the observational facts that high-redshift star clusters are more compact and massive, we speculate that the optimal parameter space for MP formation obtained in our study has a higher degree of overlap with the progenitor molecular clouds of high-z stellar clumps, which suggests that the unique environment of high-redshift star formation might play a crucial role in explaining how MPs form, and why they no longer form today.

In summary, we conclude that a successful multi-generation scenario of MP formation should involve both rapid polluters($\lesssim 5$ Myr) and the capability to lose a significant fraction($\sim 90\%$) of 1P stars. We predict that in the early universe, the typical initial surface density of GMCs that serve as GC precursors should be close to their Eddington surface density—at least closer than that of GMCs in the nearby universe. In future work, we will use the optimal parameter space for second-generation star formation derived in this study to set the initial surface density of GMCs, investigating the formation of multiple stellar populations in globular clusters under different dynamical environments.

GHL is grateful to xxx We thank the referee, We acknowledge the support from All simulations were conducted on The results presented here were produced using the

APPENDIX

A. TABLES OF FITTING PARAMETERS

The Coefficient a_i is polynomal fitted by metallicity in solar $\zeta \equiv \log_{10}(Z/0.02)$, and the coefficients are listed in Table 2. See Sec.2.1 for details.

Table 2. Coefficient of $t_{\rm BGB}$

	ζ^0	ζ^1	ζ^2	ζ^3
a_1	1593.890	2053.038	1231.226	232.7785
a_2	2706.708	1483.131	577.2723	7.411230
a_3	146.6143	-104.8442	-6.795374	-1.391127
a_4	0.04141960	0.04564888	0.02958542	0.005571483
a_5	0.3426349	—	—	—

B. INSTANTANEOUS MIXING YIELD MODEL

This section mainly demonstrate the analytical model of the formation of multiple populations in globular clusters. The model is based on the mass evolution of gas, stars and enriched gas(represented by Na in our work):

$$\begin{aligned}\frac{dM_{yield}}{dt} &= \eta \mathrm{DM}(t - t_{ylag}) \\ \frac{dM_\star}{dt} &= \mathrm{sfr}(t) \\ \frac{dM_{gas}}{dt} &= -\frac{dM_\star}{dt} - \mathscr{R}_{exp} + \frac{dM_{yield}}{dt} \\ \frac{dM_{Na}}{dt} &= -\frac{M_{Na}}{M_{gas}}\left(\frac{dM_\star}{dt} + \mathscr{R}_{exp}\right) + X_{Na,mean}\frac{dM_{yield}}{dt}\end{aligned} \tag{B1}$$

where $M_{yield}, M_\star, M_{gas}, M_{Na}$ are total stellar ejecta mass, stellar mass, gas mass within largrangian radius and Na enrichment mass, respectively. $X_{Na,ex}$ is the mean mass fraction of Na in the yield table, for binary yield it is about 4×10^{-6}. $\mathscr{R}_{exp}$ is the instantaneous gas expulsion rate, $\mathrm{DM}(t - t_{\mathrm{ylag}})$ is the dying mass as a function of present time t and enrichment timescale t_{ylag}, here we define

$$\mathrm{DM}(t - t_{\mathrm{ylag}}) = \mathrm{sfr}(t - t_{\mathrm{ylag}})$$

$\mathrm{sfr}(t)$ is a triangle-shape and integrated-SFE-normalized star formation efficiency function:

$$\mathrm{sfr}(t) = \begin{cases} \frac{\varepsilon_{\mathrm{int}}\mathrm{M_{cl}}}{t_{\mathrm{p}} - t_{\mathrm{s}}}(t - t_{\mathrm{s}}) & , t_{\mathrm{s}} < t \leq t_{\mathrm{p}} \\ \frac{\varepsilon_{\mathrm{int}}\mathrm{M_{cl}}}{t_{\mathrm{p}} - t_{\mathrm{s}}}(2t_{\mathrm{p}} - t_{\mathrm{s}} - t) & , t_{\mathrm{p}} < t \leq 2t_{\mathrm{p}} - t_{\mathrm{s}} \\ 0 & , \mathrm{else} \end{cases} \tag{B2}$$

, where t_s,t_p and t_e are the time when star formation starts, peaks and ends, respectively. With gas expulsion(e.g. Krause et al. 2016; Silich & Tenorio-Tagle 2017; Goodwin & Bastian 2006), star formation histories(Li et al. 2019; Ostriker & Kim 2022; Grudić et al. 2018), and pollution timescale models equipped, in principle we are able to calculate a variation of elements abundance we are interested in. If assume the enriched gas is completely mixed with pristine gas once it is released, the spread of Na in stars will rely on their formation time t and the instantaneous mass fraction of Na $M_{Na}(t)/M_{gas}(t)$. Therefore, Na distribution in stars can be derived by:

$$P(X_{\mathrm{Na},\star} = X_{\mathrm{Na}}) = \mathrm{sfr}(t) X_{\mathrm{Na,gas}}(t)$$

then we can derive the upper limit of chemical difference $\Delta[\mathrm{Na/Fe}]_{\mathrm{ex}}$ using the dilution model(Ricardo J. Vaca et al. 2024; Prantzos & Charbonnel 2006):

$$[\mathbf{el}/\mathbf{Fe}](\mathbf{f}) = \log_{10}\left[(1 - \mathbf{f}) \cdot 10^{[\mathrm{el}/\mathbf{Fe}]_{P2}} + \mathbf{f} \cdot \mathbf{10}^{[\mathrm{el}/\mathbf{Fe}]_{P1}}\right]$$

where

$$\mathbf{f} = 1 - \frac{M_{Na}}{M_{gas}X_{init,Na} + M_{Na}}$$

. Using exponential gas expulsion(also used by Dinnbier & Walch 2020; Kroupa et al. 2001; Dinnbier & Kroupa 2020; Brinkmann et al. 2017)[4] and triangular-shape star formation histories(Li et al. 2019; Ostriker & Kim 2022; Grudić et al. 2018) model yields typically $\sim \frac{1}{3}$ Na extrema variation in simulations. Shi et al. (2025) develop similar model to ours.

REFERENCES

Adamo, A., Bradley, L. D., Vanzella, E., et al. 2024, Nature, 632, 513, doi: 10.1038/s41586-024-07703-7

[4] this formula could not well fit the gas evolution of our simulations due to the simplifying assumption neglects the radiation-pressure dominated initial phase of gas expansion(Brinkmann et al. 2017)

Aros, F. I., Vesperini, E., & Dalessandro, E. 2025, Astronomy & Astrophysics, 699, A44, doi: 10.1051/0004-6361/202453155

Bastian, N., Cabrera-Ziri, I., & Salaris, M. 2015, Monthly Notices of the Royal Astronomical Society, 449, 3333, doi: 10.1093/mnras/stv543

Bastian, N., Lamers, H. J. G. L. M., De Mink, S. E., et al. 2013, Monthly Notices of the Royal Astronomical Society, 436, 2398, doi: 10.1093/mnras/stt1745

Bastian, N., & Lardo, C. 2018, Annual Review of Astronomy and Astrophysics, 56, 83, doi: 10.1146/annurev-astro-081817-051839

Batchelor, George Keith. 1953, The Theory of Homogeneous Turbulence (Cambridge university press)

Baumgardt, H., & Hilker, M. 2018, Monthly Notices of the Royal Astronomical Society, 478, 1520

Baumgardt, H., & Kroupa, P. 2007, Monthly Notices of the Royal Astronomical Society, 380, 1589, doi: 10.1111/j.1365-2966.2007.12209.x

Birka Zimmermann, Walch, S., Clarke, S. D., Wünsch, R., & Klepitko, A. 2025, Monthly Notices of the Royal Astronomical Society, 544, 2136, doi: 10.1093/mnras/staf1868

Brinkmann, N., Banerjee, S., Motwani, B., & Kroupa, P. 2017, Astronomy & Astrophysics, 600, A49, doi: 10.1051/0004-6361/201629312

Brown, G., & Gnedin, O. Y. 2021, Monthly Notices of the Royal Astronomical Society, 508, 5935, doi: 10.1093/mnras/stab2907

Carretta, E., Bragaglia, A., Gratton, R. G., et al. 2009, Astronomy & Astrophysics, 505, 117, doi: 10.1051/0004-6361/200912096

Charlie, C., & Spergel, D. N. 2011, The Astrophysical Journal, 726, 36, doi: 10.1088/0004-637X/726/1/36

Chen, X., Liu, Z., & Han, Z. 2024, Progress in Particle and Nuclear Physics, 134, 104083, doi: 10.1016/j.ppnp.2023.104083

Claeyssens, A., Adamo, A., Richard, J., et al. 2023, Monthly Notices of the Royal Astronomical Society, 520, 2180, doi: 10.1093/mnras/stac3791

Colbrook, M. J., Ma, X., Hopkins, P. F., & Squire, J. 2017, Monthly Notices of the Royal Astronomical Society, 467, 2421, doi: 10.1093/mnras/stx261

Cournoyer-Cloutier, C., Tran, A., Lewis, S., et al. 2021, Monthly Notices of the Royal Astronomical Society, 501, 4464, doi: 10.1093/mnras/staa3902

Cournoyer-Cloutier, C., Sills, A., Harris, W. E., et al. 2024, Massive Star Cluster Formation with Binaries. I. Evolution of Binary Populations, arXiv. https://arxiv.org/abs/2410.07433

Csengeri, T., Bontemps, S., Wyrowski, F., et al. 2017, Astronomy & Astrophysics, 600, L10

Curl, R. L. 1963, AIChE journal, 9, 175

De Mink, S. E., Pols, O. R., Langer, N., & Izzard, R. G. 2009, Astronomy & Astrophysics, 507, L1, doi: 10.1051/0004-6361/200913205

Deng, Y., Li, H., Kannan, R., et al. 2023, Monthly Notices of the Royal Astronomical Society, 527, 478, doi: 10.1093/mnras/stad3202

Deng, Y., Li, H., Liu, B., et al. 2024, RIGEL: Simulating Dwarf Galaxies at Solar Mass Resolution with Radiative Transfer and Feedback from Individual Massive Stars, arXiv. https://arxiv.org/abs/2405.08869

Denissenkov, P. A., & Hartwick, F. D. A. 2013, Monthly Notices of the Royal Astronomical Society: Letters, 437, L21, doi: 10.1093/mnrasl/slt133

D'Ercole, A., D'Antona, F., Ventura, P., Vesperini, E., & McMillan, S. L. W. 2010, Monthly Notices of the Royal Astronomical Society, 407, 854, doi: 10.1111/j.1365-2966.2010.16996.x

D'Ercole, A., Vesperini, E., D'Antona, F., McMillan, S. L. W., & Recchi, S. 2008, Monthly Notices of the Royal Astronomical Society, 391, 825, doi: 10.1111/j.1365-2966.2008.13915.x

Dinnbier, F., & Kroupa, P. 2020, Astronomy & Astrophysics, 640, A84, doi: 10.1051/0004-6361/201936570

Dinnbier, F., & Walch, S. 2020, Monthly Notices of the Royal Astronomical Society, 499, 748, doi: 10.1093/mnras/staa2560

Doherty, C. L., Gil-Pons, P., Lau, H. H. B., et al. 2014, Monthly Notices of the Royal Astronomical Society, 441, 582, doi: 10.1093/mnras/stu571

Fall, S. M., Krumholz, M. R., & Matzner, C. D. 2010, The Astrophysical Journal, 710, L142, doi: 10.1088/2041-8205/710/2/L142

Farmer, R., Laplace, E., Ma, J.-z., De Mink, S. E., & Justham, S. 2023, The Astrophysical Journal, 948, 111, doi: 10.3847/1538-4357/acc315

Fukui, Y., Habe, A., Inoue, T., Enokiya, R., & Tachihara, K. 2020, Cloud-Cloud Collisions and Triggered Star Formation, doi: 10.1093/pasj/psaa103

Ge, H., Hjellming, M. S., Webbink, R. F., Chen, X., & Han, Z. 2010, 717

Ge, H., Webbink, R. F., Chen, X., & Han, Z. 2020a, The Astrophysical Journal, 899, 132, doi: 10.3847/1538-4357/aba7b7

Ge, H., Webbink, R. F., & Han, Z. 2020b, The Astrophysical Journal Supplement Series, 249, 9, doi: 10.3847/1538-4365/ab98f6

Ge, H., Tout, C. A., Chen, X., et al. 2024, The Astrophysical Journal, 975, 254, doi: 10.3847/1538-4357/ad7ea6

Georgy, C., Ekström, S., Granada, A., et al. 2013, Astronomy & Astrophysics, 553, A24, doi: 10.1051/0004-6361/201220558

Gieles, M., Charbonnel, C., Krause, M. G. H., et al. 2018, Monthly Notices of the Royal Astronomical Society, 478, 2461, doi: 10.1093/mnras/sty1059

Glebbeek, E., Gaburov, E., Portegies Zwart, S., & Pols, O. R. 2013, Monthly Notices of the Royal Astronomical Society, 434, 3497, doi: 10.1093/mnras/stt1268

Glebbeek, E., Pols, O. R., & Hurley, J. R. 2008, Astronomy & Astrophysics, 488, 1007, doi: 10.1051/0004-6361:200809930

Glen H Hunter, Clark, P. C., Glover, S. C. O., & Klessen, R. S. 2023, Monthly Notices of the Royal Astronomical Society, 519, 4152, doi: 10.1093/mnras/stac3751

Gnedin, N. Y., & Abel, T. 2001, New Astronomy, 6, 437, doi: 10.1016/S1384-1076(01)00068-9

Goodwin, S. P., & Bastian, N. 2006, Monthly Notices of the Royal Astronomical Society, 373, 752, doi: 10.1111/j.1365-2966.2006.11078.x

Gratton, R., Bragaglia, A., Carretta, E., et al. 2019, The Astronomy and Astrophysics Review, 27, 8, doi: 10.1007/s00159-019-0119-3

Gratton, R., Sneden, C., & Carretta, E. 2004, Annual Review of Astronomy and Astrophysics, 42, 385, doi: 10.1146/annurev.astro.42.053102.133945

Grudić, M. Y., Hopkins, P. F., Faucher-Giguère, C.-A., et al. 2018, Monthly Notices of the Royal Astronomical Society, 475, 3511, doi: 10.1093/mnras/sty035

Grudić, M. Y., & Guszejnov, D. 2021, MakeCloud, 1.0. https://github.com/mikegrudic/MakeCloud

Gutcke, T. A., Pakmor, R., Naab, T., & Springel, V. 2021, Monthly Notices of the Royal Astronomical Society, staa3875, doi: 10.1093/mnras/staa3875

Heger, A., Fryer, C. L., Woosley, S. E., Langer, N., & Hartmann, D. H. 2003, The Astrophysical Journal, 591, 288, doi: 10.1086/375341

Heger, A., & Woosley, S. E. 2002, The Astrophysical Journal, 567, 532

Howard, C. S., Pudritz, R. E., Sills, A., & Harris, W. E. 2019

Hu, Y. 2025, The Astrophysical Journal, 986, 62, doi: 10.3847/1538-4357/add731

Hurley, J. R., Pols, O. R., & Tout, C. A. 2000, Monthly Notices of the Royal Astronomical Society, 315, 543, doi: 10.1046/j.1365-8711.2000.03426.x

Janicka, J., Kolbe, W., & Kollmann, W. 1979

Jenny J. Kim, & Lee, Y.-W. 2018, The Astrophysical Journal, 869, 35, doi: 10.3847/1538-4357/aaec67

Jeong, T. B., Jeon, M., Song, H., & Bromm, V. 2024, Simulating High-Redshift Galaxies: Enhancing UV Luminosity with Star Formation Efficiency and a Top-Heavy IMF, arXiv, doi: 10.48550/arXiv.2411.17007

Julia Roman-Duval, Jackson, J. M., Heyer, M., Rathborne, J., & Simon, R. 2010, The Astrophysical Journal, 723, 492, doi: 10.1088/0004-637X/723/1/492

Khurshid, S., & Donzis, D. A. 2019, Physics of Fluids, 31, 015103, doi: 10.1063/1.5080369

Krause, M. 2003, Astronomy & Astrophysics, 398, 113, doi: 10.1051/0004-6361:20021649

Krause, M. G. H., Charbonnel, C., Bastian, N., & Diehl, R. 2016, Astronomy & Astrophysics, 587, A53, doi: 10.1051/0004-6361/201526685

Kroupa, P., Aarseth, S., & Hurley, J. 2001, Monthly Notices of the Royal Astronomical Society, 321, 699, doi: 10.1046/j.1365-8711.2001.04050.x

Lacchin, E., Mastrobuono-Battisti, A., Calura, F., et al. 2024, Astronomy & Astrophysics, 681, A45, doi: 10.1051/0004-6361/202347268

Lachlan Lancaster, Ostriker, E. C., Kim, J.-G., & Kim, C.-G. 2021, The Astrophysical Journal, 914, 90, doi: 10.3847/1538-4357/abf8ac

Lahén, N., Naab, T., & Szécsi, D. 2024, Star Clusters Forming in a Low Metallicity Starburst – Rapid Self-Enrichment by (Very) Massive Stars, arXiv. https://arxiv.org/abs/2402.09518

Lahén, N., Naab, T., Kauffmann, G., et al. 2023, Monthly Notices of the Royal Astronomical Society, 522, 3092, doi: 10.1093/mnras/stad1147

Lancaster, L., Ostriker, E. C., Kim, J.-G., & Kim, C.-G. 2021a, The Astrophysical Journal Letters, 922, L3, doi: 10.3847/2041-8213/ac3333

—. 2021b, The Astrophysical Journal, 914, 89, doi: 10.3847/1538-4357/abf8ab

Laplace, E., Justham, S., Renzo, M., et al. 2021, Astronomy & Astrophysics, 656, A58, doi: 10.1051/0004-6361/202140506

Li, H., Vogelsberger, M., Marinacci, F., & Gnedin, O. Y. 2019, Monthly Notices of the Royal Astronomical Society, 487, 364, doi: 10.1093/mnras/stz1271

Li, J., Liu, C., Zhang, Z.-Y., et al. 2023, Nature, 613, 460, doi: 10.1038/s41586-022-05488-1

Limongi, M., & Chieffi, A. 2018, The Astrophysical Journal Supplement Series, 237, 13, doi: 10.3847/1538-4365/aacb24

Liubin Pan. ????

Liubin Pan, & Scannapieco, E. 2010, The Astrophysical Journal, 721, 1765, doi: 10.1088/0004-637X/721/2/1765

Livernois, A. R., Aros, F. I., Vesperini, E., et al. 2024, Energy Equipartition in Multiple-Population Globular Clusters, doi: 10.1093/mnras/stae2222

Lynnette M. Dray, & Christopher A. Tout. 2007, Monthly Notices of the Royal Astronomical Society, 376, 61, doi: 10.1111/j.1365-2966.2007.11431.x

Maity, A. K., Inoue, T., Fukui, Y., et al. 2024, Cloud-Cloud Collision: Formation of Hub-Filament Systems and Associated Gas Kinematics; Mass-collecting Cone: A New Signature of Cloud-Cloud Collision, arXiv, doi: 10.48550/arXiv.2408.06826

Matzner, C. D. 2024, The Astrophysical Journal Letters, 975, L17, doi: 10.3847/2041-8213/ad85d4

McKee, C. F., & Ostriker, E. C. 2007, Annual Review of Astronomy and Astrophysics, 45, 565, doi: 10.1146/annurev.astro.45.051806.110602

Michelle Nguyen, & Sills, A. 2024, Massive Interacting Binaries as an Enrichment Source for Multiple Populations in Star Clusters, arXiv. https://arxiv.org/abs/2405.05687

Milone, A. P., & Marino, A. F. 2022, Multiple Populations in Star Clusters, arXiv. https://arxiv.org/abs/2206.10564

Milone, A. P., Marino, A. F., Da Costa, G. S., et al. 2020, Monthly Notices of the Royal Astronomical Society, 491, 515, doi: 10.1093/mnras/stz2999

Moe, M., & Di Stefano, R. 2017, The Astrophysical Journal Supplement Series, 230, 15, doi: 10.3847/1538-4365/aa6fb6

Murray, D. W., Chang, P., Murray, N. W., & Pittman, J. 2017, Monthly Notices of the Royal Astronomical Society, 465, 1316, doi: 10.1093/mnras/stw2796

Murray, N., & Chang, P. 2015, The Astrophysical Journal, 804, 44, doi: 10.1088/0004-637X/804/1/44

Nandal, D., Sibony, Y., & Tsiatsiou, S. 2024, Fast-Rotating Massive Population~III Stars as Possible Sources of Extreme N-enrichment in High-Redshift Galaxies, arXiv. https://arxiv.org/abs/2405.11235

Ni, Y., Li, H., Vogelsberger, M., et al. 2025, Astronomy & Astrophysics, 699, A282, doi: 10.1051/0004-6361/202554126

Ostriker, E. C., & Kim, C.-G. 2022, The Astrophysical Journal, 936, 137, doi: 10.3847/1538-4357/ac7de2

Ostriker, E. C., & Shetty, R. 2011, The Astrophysical Journal, 731, 41, doi: 10.1088/0004-637X/731/1/41

Pan, L. 2008, Turbulent mixing of chemical elements in galaxies (The University of Texas at Austin)

Pan, L., Scannapieco, E., & Scalo, J. 2012, Journal of Fluid Mechanics, 700, 459–489, doi: 10.1017/jfm.2012.143

Paxton, B., Smolec, R., Schwab, J., et al. 2019, The Astrophysical Journal Supplement Series, 243, 10, doi: 10.3847/1538-4365/ab2241

Poelarends, A. J. T., Wurtz, S., Tarka, J., Adams, L. C., & Hills, S. T. 2017, The Astrophysical Journal, 850, 197, doi: 10.3847/1538-4357/aa988a

Prantzos, N., & Charbonnel, C. 2006, Astronomy & Astrophysics, 458, 135, doi: 10.1051/0004-6361:20065374

Raffaele G. Gratton, Carretta, E., & Bragaglia, A. 2012, The Astronomy and Astrophysics Review, 20, 50, doi: 10.1007/s00159-012-0050-3

Ralf S. Klessen, & Lin, D. N. C. 2003, Physical Review E, 67, 046311, doi: 10.1103/PhysRevE.67.046311

Raskutti, S., Ostriker, E. C., & Skinner, M. A. 2016, The Astrophysical Journal, 829, 130, doi: 10.3847/0004-637X/829/2/130

Renaud, F. 2018, New Astronomy Reviews

Renzini, A., D'Antona, F., Cassisi, S., et al. 2015, Monthly Notices of the Royal Astronomical Society, 454, 4197, doi: 10.1093/mnras/stv2268

Ricardo J. Vaca, Cabrera-Ziri, I., C, G. M., Bastian, N., & Salaris, M. 2024, Astronomy & Astrophysics, 690, A199, doi: 10.1051/0004-6361/202451285

Rice, T. S., Goodman, A. A., Bergin, E. A., Beaumont, C., & Dame, T. M. 2016, The Astrophysical Journal, 822, 52, doi: 10.3847/0004-637X/822/1/52

Robert G. Izzard, & Tout, C. A. 2003, Publications of the Astronomical Society of Australia, 20, 345, doi: 10.1071/AS03026

Rosdahl, J., Blaizot, J., Aubert, D., Stranex, T., & Teyssier, R. 2013, Monthly Notices of the Royal Astronomical Society, 436, 2188, doi: 10.1093/mnras/stt1722

S. E. De Mink, Langer, N., Izzard, R. G., Sana, H., & De Koter, A. 2013, The Astrophysical Journal, 764, 166, doi: 10.1088/0004-637X/764/2/166

Schneider, F. R. N., Podsiadlowski, Ph., Langer, N., Castro, N., & Fossati, L. 2016, Monthly Notices of the Royal Astronomical Society, 457, 2355, doi: 10.1093/mnras/stw148

Shi, Y., Dai, L., Murray, N., et al. 2025, Very Massive Stars and High N/O: A Tale of the Nitrogen-enriched Super Star Cluster in the Sunburst Arc, arXiv, doi: 10.48550/arXiv.2510.15823

Silich, S., & Tenorio-Tagle, G. 2017, Monthly Notices of the Royal Astronomical Society, 465, 1375, doi: 10.1093/mnras/stw2879

Soberman, G. E., & Phinney, E. S. ????

Springel, V. 2010, Monthly Notices of the Royal Astronomical Society, 401, 791, doi: 10.1111/j.1365-2966.2009.15715.x

Steinwandel, U. P., & Goldberg, J. A. 2025, The Astrophysical Journal, 979, 44, doi: 10.3847/1538-4357/ad98ea

Temmink, K. D., Pols, O. R., Justham, S., Istrate, A. G., & Toonen, S. 2023, Astronomy & Astrophysics, 669, A45, doi: 10.1051/0004-6361/202244137

Thompson, T. A., & Krumholz, M. R. 2016, Monthly Notices of the Royal Astronomical Society, 455, 334, doi: 10.1093/mnras/stv2331

Topping, M. W., Stark, D. P., Senchyna, P., et al. 2024, Monthly Notices of the Royal Astronomical Society, 529, 3301, doi: 10.1093/mnras/stae682

—. 2025, The Astrophysical Journal, 980, 225, doi: 10.3847/1538-4357/ada95c

Torrey, P., Vogelsberger, M., Sijacki, D., Springel, V., & Hernquist, L. 2012, Monthly Notices of the Royal Astronomical Society, 427, 2224

Van Den Heuvel, E. P. J. 1969, The Astronomical Journal, 74, 1095, doi: 10.1086/110909

Vartanyan, D., Laplace, E., Renzo, M., et al. 2021, The Astrophysical Journal Letters, 916, L5, doi: 10.3847/2041-8213/ac0b42

Ventura, P., & D'Antona, F. 2009, Astronomy & Astrophysics, 499, 835, doi: 10.1051/0004-6361/200811139

Vesperini, E., McMillan, S. L. W., D'Antona, F., & D'Ercole, A. 2010, The Astrophysical Journal, 718, L112, doi: 10.1088/2041-8205/718/2/L112

—. 2013, Monthly Notices of the Royal Astronomical Society, 429, 1913, doi: 10.1093/mnras/sts434

Vink, J. S. 2023, Astronomy & Astrophysics, 679, L9, doi: 10.1051/0004-6361/202347827

Vogelsberger, M., Genel, S., Sijacki, D., et al. 2013, Monthly Notices of the Royal Astronomical Society, 436, 3031, doi: 10.1093/mnras/stt1789

Wagg, T., Dalcanton, J. J., Renzo, M., et al. 2025, Delayed and Displaced: The Impact of Binary Interactions on Core-collapse SN Feedback, arXiv, doi: 10.48550/arXiv.2504.17903

Wayne Osborn. 1971, The Observatory, 91, 223

Weinberger, R., Springel, V., & Pakmor, R. 2020, The Astrophysical Journal Supplement Series, 248, 32, doi: 10.3847/1538-4365/ab908c

Wu, B., Loo, S. V., Tan, J. C., & Bruderer, S. 2015, The Astrophysical Journal, 811, 56, doi: 10.1088/0004-637X/811/1/56

Wu, B., Tan, J. C., Nakamura, F., et al. 2017, The Astrophysical Journal, 835, 137, doi: 10.3847/1538-4357/835/2/137

Xu, S., & Lazarian, A. 2020, The Astrophysical Journal, 890, 157, doi: 10.3847/1538-4357/ab6e63

Xu, X.-T., Schürmann, C., Langer, N., et al. 2025, Populations of Evolved Massive Binary Stars in the Small Magellanic Cloud I: Predictions from Detailed Evolution Models, arXiv, doi: 10.48550/arXiv.2503.23876

Yates, R. M., Hendriks, D., Vijayan, A. P., et al. 2023, Monthly Notices of the Royal Astronomical Society, 527, 6292, doi: 10.1093/mnras/stad3419

Yoon, S.-C. 2015

Yoon, S.-C., Woosley, S. E., & Langer, N. 2010, The Astrophysical Journal, 725, 940, doi: 10.1088/0004-637X/725/1/940